Acta Cryst A FOUNDATIONS ADVANCES

ISSN 2053-2733

Shape transform phasing of edgy nanocrystals

J. P. J. Chen,[a] J. J. Donatelli,[b,c] K. E. Schmidt[a] and R. A. Kirian[a]*

[a]Department of Physics, Arizona State University, Tempe, AZ 85287, USA, [b]Center for Advanced Mathematics for Energy Research Applications, Lawrence Berkeley National Laboratory, Berkeley, CA 94720, USA, and [c]Department of Applied Mathematics, Lawrence Berkeley National Laboratory, Berkeley, CA 94720, USA. *Correspondence e-mail: rkirian@asu.edu

Received 7 November 2018
Accepted 22 January 2019

Edited by A. Altomare, Institute of Crystallography - CNR, Bari, Italy

Keywords: iterative projection algorithms; shape transforms; shape transform phasing; phase retrieval; nanocrystals; serial femtosecond crystallography; X-ray free-electron lasers.

Diffraction patterns from small protein crystals illuminated by highly coherent X-rays often contain measurable interference signals between Bragg peaks. This coherent 'shape transform' signal introduces enough additional information to allow the molecular densities to be determined from the diffracted intensities directly, without prior information or resolution restrictions. However, the various correlations amongst molecular occupancies/vacancies at the crystal surface result in a subtle yet critical problem in shape transform phasing whereby the sublattices of symmetry-related molecules exhibit a form of partial coherence amongst lattice sites when an average is taken over many crystal patterns. Here an iterative phase retrieval algorithm is developed which is capable of treating this problem; it is demonstrated on simulated data.

1. Introduction

The method of serial femtosecond crystallography (Chapman *et al.*, 2011) emerged soon after the startup of the world's first hard-X-ray free-electron laser (XFEL) in 2009 (Emma *et al.*, 2010). The extreme intensity of XFEL pulses enabled room-temperature crystallography on protein crystals of sub-micrometre sizes, with the option of triggering dynamics by various means such as light activation, while at the same time avoiding nearly all signs of X-ray radiation damage which often limits resolution or leads to unwanted artifacts in electron-density maps. As reviewed elsewhere, XFELs allow a wide range of protein crystallography studies that appear to be impossible with current synchrotron facilities (Schlichting, 2015; Spence, 2017; Zatsepin, 2018).

In serial femtosecond crystallography, large numbers of crystal diffraction patterns, sometimes exceeding a million, are combined to form a single, 3D set of crystallographic structure-factor amplitudes by merging Bragg reflection intensities. As with conventional crystallography, the structure-factor phases are unmeasured yet necessary to form the real-space electron-density maps. It has now been established that most, if not all, conventional crystallographic phase retrieval techniques are effective on XFEL diffraction data (Schlichting, 2017), including those that rely on anomalous diffraction near resonant conditions. In addition to conventional techniques, a number of new phase retrieval principles have emerged during the development of serial femtosecond crystallography (Son *et al.*, 2011; Ayyer *et al.*, 2016).

The phase retrieval method that we explore here is often referred to as 'shape transform phasing', as it makes use of the additional information contained in so-called shape transform intensities seen *between* Bragg reflections when finite crystals are exposed to coherent light (Kirian *et al.*, 2010; Spence *et al.*, 2011; Chen *et al.*, 2014*a*). By 'shape transforms' we literally

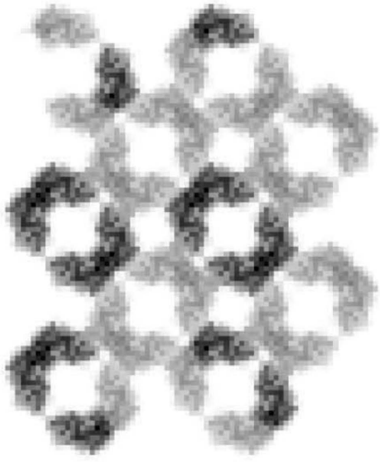

mean the Fourier transform of the shape of the crystal, where, mathematically, the shape of a crystal is given by a binary function that has a 1 where a crystal lattice point is occupied by a molecule and 0 where the lattice point is not occupied. Section 2 contains more details on this model. Shape transforms from protein crystals can be observed with a synchrotron X-ray source (Boutet & Robinson, 2008), but are rare because most synchrotron-based crystallography instruments do not provide coherence lengths that span the entire crystal, and/or the fluence is usually too low because of the fundamental limitations imposed by radiation damage. The emergence of intense, laser-like X-ray beams produced by XFELs, which circumvent the effects of radiation damage in the measurements by using femtosecond pulses, greatly improved the visibility of shape transforms (Chapman *et al.*, 2011). An example diffraction pattern collected during the first serial femtosecond X-ray crystallography experiment is shown in Fig. 1. In addition, increased data rates further improved the extent that inter-Bragg signals can be seen in many data sets upon averaging in the continuum of 3D reciprocal-space locations (Yefanov *et al.*, 2014). Observations of high-contrast shape transforms at XFELs triggered many studies on the theory of shape transform phasing (Spence *et al.*, 2011; Elser, 2013; Liu *et al.*, 2014; Chen *et al.*, 2014*a*,*b*, 2016; Chen & Millane, 2014; Kirian *et al.*, 2014, 2015; Millane & Chen, 2014), but the only experimental results published so far are limited to artificial 2D crystals (Kirian *et al.*, 2015).

The basic notion of solving the crystallographic phase problem by sampling intensities between Bragg reflections was first proposed in the crystallography literature by Sayre (1952). Experimental efforts were made by Perutz and colleagues in the 1950s to determine intensities between the nominal Bragg reflections by exploiting the variation in unit-cell dimensions upon crystal swelling (Green *et al.*, 1954). Shape transform phasing is similar in spirit to those early efforts, in the sense that it also exploits additional samples of the underlying molecular transform. This additional information comes at the cost of requiring sufficiently small crystals, highly coherent X-ray sources and perhaps larger volumes of data, but is nonetheless of significant interest because, in principle, it would allow for the solution of the phase problem without prior-known information, and without restrictions on the resolution of the data. In addition to its potential to solve difficult phase problems in protein crystallography, the development of shape transform phasing calls for generalizations of the phase retrieval problem and may find other applications in problems of a similar mathematical form. One immediate generalization would include a model for the diffuse diffraction associated with translational disorder, which has recently been used as a means of extending the resolution of density maps (Ayyer *et al.*, 2016).

The absence of experimental shape transform phasing results for protein samples is in part due to the lack of a generalized phase retrieval algorithm which can accommodate a subtle, yet critical, problem that arises due to variations in molecular occupancies at the surfaces of crystals (Elser, 2013; Kirian *et al.*, 2014; Chen & Millane, 2014; Williams *et al.*, 2017). It is natural to describe the problem as the result of 'incomplete unit cells' at the surface of the crystal, but we warn that the 'unit cell' is an elusive concept for finite crystals. For example, in 1D, there are a total of four types of finite crystal arrangements for two molecules, A and B, as shown in Fig. 2. However only two of the four possible crystal types have a well-defined unit cell, consisting of the molecular configurations AB and BA. In a viewpoint which we take below, the intensities averaged over many such crystals are equivalent to those from a partially coherent target or illumination source, roughly similar to the work by Dilanian *et al.* (2013). We model the truncation effects arising inevitably on the edges of finite crystals as occupancies of molecules on an infinite lattice. Some attempts have been made to develop methods that can accommodate the edge occupancy problem in shape

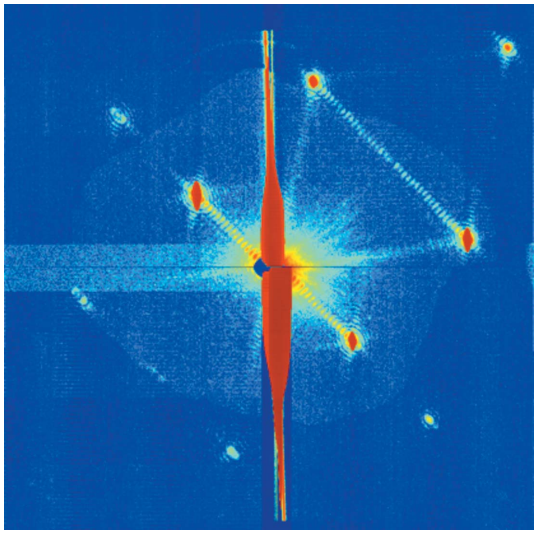

Figure 1
A single raw diffraction pattern, *i.e.* without any pixel masking or background subtraction, obtained at the Linac Coherent Light Source from a sub-micrometre crystal of Photosystem I (Chapman *et al.*, 2011). The interference fringes between Bragg reflections provide sufficient sampling of the molecular transform to solve the phase problem in principle. The red streak running vertically through the center of the pattern is the scattering of X-rays from the edge of the water jet that carried the crystals into the XFEL pulses.

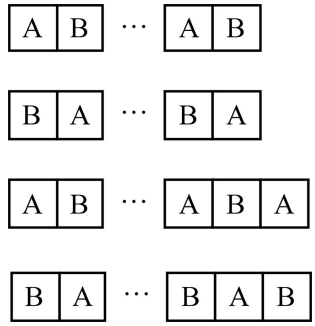

Figure 2
The four possible types of crystals consisting of two kinds of molecules in 1D.

transform phasing (Kirian *et al.*, 2014; Chen *et al.*, 2016), but these methods have been limited to idealizations and approximations that are not likely to be effective on experimental data.

In this article, we demonstrate an algorithm that solves the general problem of shape transform phasing for crystals with arbitrary molecular occupancies. We first describe a diffraction model that accommodates missing molecules on the edge of, and potentially within, finite crystals. Then, after describing the basic ideas behind the application of iterative projection algorithms to the problem of phase retrieval, we propose a modified iterative projection algorithm that solves the phase problem when the input intensity data are the 3D average over coherent finite crystal diffraction intensities. We allow for any types of molecular occupancies and provide simulation results that demonstrate the algorithm for 2D and 3D crystals. We conclude with a discussion of our findings and potential extensions to the algorithm including how some other types of crystal disorder could be accounted for in our diffraction model and phase retrieval algorithm.

2. Finite crystal model

In this section we construct a mathematical model that describes occupancies of objects (molecules) on a lattice. The specific goal is to model the occurrence of molecules on the surface of a finite crystal giving rise to irregular surface terminations. We note here that the particular model we formulate, along with our proposed reconstruction algorithm, can handle arbitrary occupancies on a lattice in general and need not be restricted to lattice occupancies describing the surface of a finite crystal. Other cases of particular interest include crystals with holes for example. The aim is to use this model to describe the ensemble-average of crystal diffraction intensities, which we take as the input to our phase retrieval algorithm.

We assume that the X-ray scattering is in the regime where there is no multiple scattering, and that the diffracted intensity is measured in the far-field. The diffracted amplitude is therefore given by the Fourier transform of a real-space density. In the first Born approximation, this real-space density is proportional to the electronic charge density. In order for our model to describe more general scattering, for example near X-ray edges, where there can be additional phase shifts, we allow the real-space density to be complex, but will continue to call it the electron or scattering density. No other kind of crystal disorder except for random occupancies of molecules on the crystal lattice is included in the model that follows.

We begin by describing a general model that expresses the averaged diffracted intensity explicitly in terms of the occupancies of the crystal lattice (Section 2.1) and then show that an equivalent model can be formulated in terms of shape transforms (Section 2.2) which has a much smaller number of parameters that are needed to capture the information in the averaged diffracted intensity.

2.1. Occupancy formulation

Consider a molecule described by an electron density $f(\mathbf{r})$ that serves as the asymmetric unit for the construction of crystals. The crystal space group consists of K symmetry-related partners in total. The kth symmetry partner is denoted by $f_k(\mathbf{r})$ and is related to $f(\mathbf{r})$ through a rotation $\mathbf{R}_k$ and spatial shift $\mathbf{s}_k$. We combine these operations into a single linear transformation, $\mathcal{L}_k$, such that

$$f_k(\mathbf{r}) = \mathcal{L}_k f(\mathbf{r}) = f\big[\mathbf{R}_k(\mathbf{r}-\mathbf{s}_k)\big] \tag{1}$$

and

$$f(\mathbf{r}) = \mathcal{L}_k^{-1} f_k(\mathbf{r}) = f_k\big(\mathbf{R}_k^{-1}\mathbf{r}+\mathbf{s}_k\big). \tag{2}$$

We denote the real-space scattering density of the nth crystal as

$$\begin{aligned} g_n(\mathbf{r}) &= \sum_{\boldsymbol{\alpha}}^{\infty}\sum_{k=1}^{K} w_{k\boldsymbol{\alpha}n} f[\mathbf{R}_k(\mathbf{r}-\mathbf{s}_k-\mathbf{r}_{\boldsymbol{\alpha}})] \\ &= \sum_{\boldsymbol{\alpha}}^{\infty}\sum_{k=1}^{K} w_{k\boldsymbol{\alpha}n} f_k(\mathbf{r}-\mathbf{r}_{\boldsymbol{\alpha}}), \end{aligned} \tag{3}$$

where the vector $\boldsymbol{\alpha}$ is a 3-tuple of integer indices $\boldsymbol{\alpha} = (\alpha_1, \alpha_2, \alpha_3)$ which identifies the real-space lattice points and the molecular occupancies $w_{k\boldsymbol{\alpha}n}$ are equal to either 0 or 1 and specify the absence or presence, respectively, of the kth molecule in the $\boldsymbol{\alpha}$th unit cell of the nth crystal. The location of those lattice points, given by the lattice vectors $\mathbf{r}_{\boldsymbol{\alpha}}$, is formed via linear combinations of the three crystal basis vectors $\mathbf{a}_1$, $\mathbf{a}_2$ and $\mathbf{a}_3$ where $\mathbf{r}_{\boldsymbol{\alpha}} = \alpha_1\mathbf{a}_1 + \alpha_2\mathbf{a}_2 + \alpha_3\mathbf{a}_3$. The notation $\sum_{\boldsymbol{\alpha}}^{\infty}$ is shorthand for $\sum_{\alpha_1=-\infty}^{\infty}\sum_{\alpha_2=-\infty}^{\infty}\sum_{\alpha_3=-\infty}^{\infty}$.

The complex diffracted amplitude of the crystal, $G_n(\mathbf{q})$, is given by the Fourier transform of the scattering density $g_n(\mathbf{r})$ and is equal to

$$\begin{aligned} G_n(\mathbf{q}) &= \sum_{\boldsymbol{\alpha}}^{\infty}\sum_{k=1}^{K} w_{k\boldsymbol{\alpha}n} \int_{-\infty}^{\infty} f_k(\mathbf{r}-\mathbf{r}_{\boldsymbol{\alpha}}) \exp(-i\mathbf{q}\cdot\mathbf{r})\,\mathrm{d}\mathbf{r} \\ &= \sum_{\boldsymbol{\alpha}}^{\infty}\sum_{k=1}^{K} w_{k\boldsymbol{\alpha}n} F_k(\mathbf{q}) \exp(-i\mathbf{q}\cdot\mathbf{r}_{\boldsymbol{\alpha}}) \end{aligned} \tag{4}$$

where

$$F_k(\mathbf{q}) = F(\mathbf{R}_k\mathbf{q}) \exp(-i\mathbf{q}\cdot\mathbf{s}_k) \tag{5}$$

and $F(\mathbf{q})$ is the Fourier transform of $f(\mathbf{r})$. The diffracted intensity is then

$$\begin{aligned} I_n(\mathbf{q}) &= |G_n(\mathbf{q})|^2 \\ &= \sum_{\boldsymbol{\alpha}}^{\infty}\sum_{\boldsymbol{\beta}}^{\infty}\sum_{k=1}^{K}\sum_{l=1}^{K} w_{k\boldsymbol{\alpha}n} w_{l\boldsymbol{\beta}n} F_l^*(\mathbf{q}) F_k(\mathbf{q}) \exp[-i\mathbf{q}\cdot(\mathbf{r}_{\boldsymbol{\alpha}}-\mathbf{r}_{\boldsymbol{\beta}})] \end{aligned} \tag{6}$$

where * denotes complex conjugation. The average diffracted intensity over an ensemble of crystals is

$$\begin{aligned} I(\mathbf{q}) &= \langle I_n(\mathbf{q})\rangle_n \\ &= \sum_{\boldsymbol{\alpha}}^{\infty}\sum_{\boldsymbol{\beta}}^{\infty}\sum_{k=1}^{K}\sum_{l=1}^{K} W_{k\boldsymbol{\alpha}l\boldsymbol{\beta}} F_l^*(\mathbf{q}) F_k(\mathbf{q}) \exp[-i\mathbf{q}\cdot(\mathbf{r}_{\boldsymbol{\alpha}}-\mathbf{r}_{\boldsymbol{\beta}})] \end{aligned} \tag{7}$$

where the term

$$W_{k\boldsymbol{\alpha}l\boldsymbol{\beta}} \equiv \langle w_{k\boldsymbol{\alpha}n} w_{l\boldsymbol{\beta}n} \rangle_n \tag{8}$$

specifies the correlations amongst molecular occupancies and will be referred to simply as the 'occupancy matrix'. Since we assume finite crystals, each unique set of indices comprised of k and $\boldsymbol{\alpha}$, which together specify a unique molecule in the crystal, may be mapped to one index. Similarly, the sets of indices comprised of l and $\boldsymbol{\beta}$ may also be mapped to a single index, and hence the occupancy matrix requires only two indices to uniquely refer to each pair of molecules. The use of a single integer index would of course be the natural choice for a non-crystalline assembly of molecules.

The number of parameters in the occupancy matrix W is of the order of the square of the total number of molecules in the largest crystal in the ensemble, and thus scales as the sixth power of the linear crystal size. As an example, the number of parameters in the occupancy matrix for a crystal with just ten unit cells on each side is of the order 10^6. Given the very large number of parameters and its unfavorable scaling with crystal size, we seek a substantial reduction in the number of unknowns in order to solve for our sought-after asymmetric unit $f(\mathbf{r})$. This might be possible through the use of a physical model for protein crystal growth as occupancy correlations are likely dependent only on local neighborhoods for example. However, a much simpler approach is to reformulate the problem as follows.

2.2. Shape transform formulation

We may view the construction of a finite crystal as the superposition of K 'sublattices' in which the kth sublattice contains molecules that have been rotated by $\mathbf{R}_k$ and translated by $\mathbf{s}_k$. Two examples of finite crystals are shown in Fig. 3. In those examples, there exist two kinds of symmetry partners ($K = 2$) and the occupied molecular sites are marked by crosses for one kind of symmetry partner (the 'P' molecule) and circles for the other kind (the 'mirrored P' molecule).

The real-space scattering density of the nth crystal can now be written as

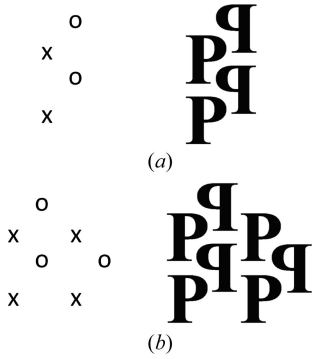

Figure 3
Two examples of finite crystals with two distinct molecular orientations ('P' and 'mirrored P') along with their occupied sublattice points (crosses and circles). (*a*) A finite crystal describable by a unit cell. (*b*) A finite crystal not describable by any non-trivial unit cell (a trivial unit cell is when the unit cell is the crystal itself).

$$g_n(\mathbf{r}) = \sum_{k=1}^{K} s_{kn}(\mathbf{r}) \otimes f_k(\mathbf{r}) \tag{9}$$

where $\otimes$ denotes the convolution operation and $s_{kn}(\mathbf{r})$ is the shape function for the kth symmetry partner in the nth crystal. The shape function is related to the occupancies by

$$s_{kn}(\mathbf{r}) = \sum_{\boldsymbol{\alpha}}^{\infty} w_{k\boldsymbol{\alpha}n} \delta(\mathbf{r} - \mathbf{r}_{\boldsymbol{\alpha}}) \tag{10}$$

where $\delta(\mathbf{r})$ is the Dirac delta function. The complex diffracted amplitudes of the nth crystal are then equal to

$$G_n(\mathbf{q}) = \sum_{k=1}^{K} S_{kn}(\mathbf{q}) F_k(\mathbf{q}) \tag{11}$$

where $S_{kn}(\mathbf{q})$ is the Fourier transform of the shape function for the kth symmetry partner in the nth crystal, given by

$$S_{kn}(\mathbf{q}) = \sum_{\boldsymbol{\alpha}}^{\infty} w_{k\boldsymbol{\alpha}n} \exp(-i\mathbf{q} \cdot \mathbf{r}_{\boldsymbol{\alpha}}). \tag{12}$$

We refer to the Fourier transform of the shape function in this article as the 'shape transform'. The diffracted intensity for the nth crystal is

$$I_n(\mathbf{q}) = |G_n(\mathbf{q})|^2 = \sum_{k=1}^{K} \sum_{l=1}^{K} S_{ln}^*(\mathbf{q}) S_{kn}(\mathbf{q}) F_l^*(\mathbf{q}) F_k(\mathbf{q}) \tag{13}$$

and the average intensity is

$$I(\mathbf{q}) = \langle I_n(\mathbf{q}) \rangle_n = \sum_{k=1}^{K} \sum_{l=1}^{K} C_{kl}(\mathbf{q}) F_l^*(\mathbf{q}) F_k(\mathbf{q}), \tag{14}$$

where

$$C_{kl}(\mathbf{q}) \equiv \langle S_{ln}^*(\mathbf{q}) S_{kn}(\mathbf{q}) \rangle_n = \sum_{\boldsymbol{\alpha}}^{\infty} \sum_{\boldsymbol{\beta}}^{\infty} W_{k\boldsymbol{\alpha}l\boldsymbol{\beta}} \exp[-i\mathbf{q} \cdot (\mathbf{r}_{\boldsymbol{\alpha}} - \mathbf{r}_{\boldsymbol{\beta}})]. \tag{15}$$

We will refer to $C_{kl}(\mathbf{q})$ as the 'averaged shape transform'. It is useful to compare equation (14) with equation (7). The above formulation effectively replaces the occupancy matrix with the average products of shape transforms $S_{kn}(\mathbf{q})$. We show in Appendix *B* that the diffracted intensity given by equation (14) allows the coarse-graining (down-sampling) of the intensity, and in turn, the averaged shape transforms, $C_{kl}(\mathbf{q})$, such that the weights $W_{k\boldsymbol{\alpha}l\boldsymbol{\beta}}$ do not need to be individually retrieved. This leads to the reduction in the number of parameters describing the shape transform phasing problem as desired.

A property of the averaged shape transforms, $C_{kl}(\mathbf{q})$, is that they are periodic upon translations of reciprocal-lattice vectors $\mathbf{g}_{\mathbf{h}}$ in reciprocal space,

$$C_{kl}(\mathbf{q} - \mathbf{g}_{\mathbf{h}}) = C_{kl}(\mathbf{q}), \tag{16}$$

where $\mathbf{g}_{\mathbf{h}}$ are the positions of the reciprocal-lattice points identified with the reciprocal-lattice vectors $\mathbf{b}_1$, $\mathbf{b}_2$ and $\mathbf{b}_3$, and a 3-tuple of integer indices $\mathbf{h} = (h_1, h_2, h_3)$ (the Miller indices) such that $\mathbf{g}_{\mathbf{h}} = h_1\mathbf{b}_1 + h_2\mathbf{b}_2 + h_3\mathbf{b}_3$. We will refer to the periodic domain in $C_{kl}(\mathbf{q})$ as the 'shape transform cell'. The shape transform cells are equivalent to the Wigner–Seitz cells and Brillouin zones in crystallography and condensed matter

physics in the sense that they all contain the same amount of information that is needed to construct $C_{kl}(\mathbf{q})$. Note that the averaged shape transform is also inversion conjugate symmetric, *i.e.*

$$C_{kl}(-\mathbf{q}) = C^*_{kl}(\mathbf{q}), \tag{17}$$

and $C_{kl}(\mathbf{q})$ are Hermitian with respect to the indices k and l, since

$$\begin{aligned} C_{kl}(\mathbf{q}) &= \langle S^*_{ln}(\mathbf{q}) S_{kn}(\mathbf{q}) \rangle_n \\ &= \left[\langle S^*_{kn}(\mathbf{q}) S_{ln}(\mathbf{q}) \rangle_n \right]^* \\ &= C^*_{lk}(\mathbf{q}), \end{aligned} \tag{18}$$

consequently implying that $C_{kk}(\mathbf{q}) = C^*_{kk}(\mathbf{q})$ which means $C_{kk}(\mathbf{q})$ is real for all $\mathbf{q}$. The periodicity and centrosymmetry of the averaged shape transforms are derived in Appendix *A*.

Equation (14) can be written in matrix notation as

$$I(\mathbf{q}) = [F^*_1(\mathbf{q}) \ldots F^*_K(\mathbf{q})] \begin{bmatrix} C_{11}(\mathbf{q}) & \ldots & C_{1K}(\mathbf{q}) \\ \vdots & & \vdots \\ C^*_{1K}(\mathbf{q}) & \ldots & C_{KK}(\mathbf{q}) \end{bmatrix} \begin{bmatrix} F_1(\mathbf{q}) \\ \vdots \\ F_K(\mathbf{q}) \end{bmatrix}, \tag{19}$$

yielding the matrix representation for the averaged diffracted intensity at a particular $\mathbf{q}$:

$$I(\mathbf{q}) = \mathbf{F}^\dagger(\mathbf{q}) \mathbf{C}(\mathbf{q}) \mathbf{F}(\mathbf{q}), \tag{20}$$

where $\mathbf{F}(\mathbf{q})$ is a K by 1 vector containing the set of complex numbers $\{F_k(\mathbf{q})\}$, $\mathbf{C}(\mathbf{q})$ is a K by K matrix containing the set of complex numbers $\{C_{kl}(\mathbf{q})\}$, and the $\dagger$ denotes conjugate transpose. Since the matrix $\mathbf{C}(\mathbf{q})$ is Hermitian, the intensities $I(\mathbf{q})$ and the diagonal elements $C_{kk}(\mathbf{q})$ will be real-valued. The matrix $\mathbf{C}(\mathbf{q})$ is also positive semi-definite since $I(\mathbf{q}) \geq 0$ for all $\mathbf{F}(\mathbf{q})$. The above properties of the averaged shape transform function, $C_{kl}(\mathbf{q})$, and the averaged shape transform matrix, $\mathbf{C}(\mathbf{q})$, will be utilized extensively in the phase retrieval process.

3. Reconstruction algorithm

The goal of the reconstruction problem is to retrieve the scattering density of the asymmetric unit $f(\mathbf{r})$, given the averaged diffraction intensity $I(\mathbf{q})$ along with some basic assumptions about $f(\mathbf{r})$ and $\mathbf{C}(\mathbf{q})$. A practical way of reconstructing $f(\mathbf{r})$ from its measured Fourier intensity $I(\mathbf{q})$ is via iterative projection algorithms (Fienup, 1982; Elser, 2003*a*; Marchesini, 2007; Millane & Lo, 2013). These algorithms are designed to solve general constraint-satisfaction problems where one is given a number of constraints that need to be simultaneously satisfied. The problem is usually parameterized such that there are D parameters and each constraint defines a set of equations in terms of those parameters, which can be interpreted geometrically as surfaces in a D-dimensional space. Solutions to the constraint-satisfaction problem are then located at the intersection of all the constraint surfaces.

To reach the intersection, one starts at any position in the D-dimensional space and explores the space by iteratively applying a fixed rule composed of so-called projection operators where the action of a single projection operation makes the smallest change to the current position in the D-dimensional space such that one of the constraints is satisfied.

Suitable combinations of these projection operators are used to iteratively update the current position in the D-dimensional space to a new position such that the intersection of all constraint surfaces, and thus the solution to the problem, may eventually be reached. Any combination of projection operators is called an iterative projection algorithm (IPA).

We first outline the projection operators for conventional phase retrieval and describe the iterative update rules that we use. These update rules are the same for the shape transform phase retrieval problem and only the projection operators are changed. These new operators for handling the averaged diffracted intensity from finite crystals with random molecular occupancies will be described thereafter.

3.1. Phase retrieval via IPAs

We define the function $f(\mathbf{r})$ that we sample at a series of discrete points. Here we take a regular grid with D grid points in total. The value of $f(\mathbf{r})$ on each grid point is viewed as an independent dimension and the full function $f(\mathbf{r})$ is given by a single point in that D-dimensional space. As mentioned previously, the measured Fourier intensity $I(\mathbf{q})$, along with constraints on the object $f(\mathbf{r})$, can be described by sets of equations that correspond to surfaces in the D-dimensional space, and we seek the point at which all constraint surfaces intersect. In the presence of measurement errors this intersection might not exist and we seek instead a point that is closest to all constraint surfaces.

The constraints in diffraction phase retrieval are almost invariably divided into two classes: those in real space and those in reciprocal space.

The main constraint in real space is the finite extent of the object, the shape of which is referred to as the object 'support'. In reciprocal space the main constraint is the measured Fourier intensity data. The corresponding projection operators in real and reciprocal space are denoted by P_S and P_M, respectively, and are defined as follows.

Let $\mathbb{S}$ be the set of all position vectors of the samples within the support of $f(\mathbf{r})$, *i.e.* $f(\mathbf{r}) = 0$ for all $\mathbf{r} \notin \mathbb{S}$. The projection operator P_S sets the value of the samples outside $\mathbb{S}$ to zero and leaves the value of the samples inside $\mathbb{S}$ unchanged. Defining a binary function $s(\mathbf{r})$ as

$$s(\mathbf{r}) = \begin{cases} 1 & \mathbf{r} \in \mathbb{S} \\ 0 & \mathbf{r} \notin \mathbb{S} \end{cases}, \tag{21}$$

the projection operator P_S is given by

$$P_S f(\mathbf{r}) = s(\mathbf{r}) f(\mathbf{r}). \tag{22}$$

The projection operator P_M takes a complex number and changes the magnitude of that complex number to the desired value, which in this case is the square root of the measured

Fourier intensity, $I_{\rm data}(\mathbf{q})$. The set of all complex numbers that have the same magnitude defines a circle on the complex plane; therefore the projection, which seeks the minimum change to the input such that it satisfies the equation for the associated constraint surface, involves scaling the input complex number such that it moves radially on the complex plane until it intersects the circle with the desired magnitude. Denoting the Fourier transform operator by $\mathcal{F}$, the projection operator P_M is

$$P_M f(\mathbf{r}) = \mathcal{F}^{-1}\left[\frac{I_{\rm data}(\mathbf{q})}{I(\mathbf{q})}\right]^{1/2}\mathcal{F}f(\mathbf{r}), \tag{23}$$

where $I(\mathbf{q}) = |\mathcal{F}f(\mathbf{r})|^2$. In simple terms, this operation sets the magnitude of the complex diffraction amplitude to the measured value, while leaving the current phase estimate unchanged.

The above projection operators can be combined to form rules that update $f(\mathbf{r})$ in such a way that it becomes closer to satisfying all of the constraints. The update rule generates the $(i+1)$th iterate from a combination of P_S, P_M and the iterate at the ith iteration, $\mathbf{x}^{(i)}$, *i.e.*

$$\mathbf{x}^{(i+1)} = \text{Rule}\left[\mathbf{x}^{(i)}, P_S, P_M\right]. \tag{24}$$

The iterate in the case of conventional diffractive imaging is $f(\mathbf{r})$ but it could in general encapsulate the entire list of entities that are allowed to change during the application of the algorithm. In the case of shape transform phasing, the iterate is comprised of $\{f_k(\mathbf{r})\}$ and $\{C_{kl}(\mathbf{q})\}$ as will be explained in more detail in the next section. When the iterate no longer changes upon application of the update rule, *i.e.* $\mathbf{x}^{(i+1)} = \mathbf{x}^{(i)}$, the algorithm is said to have reached a fixed point. Not all fixed points are solutions and they often correspond to local minima of the distance between the two constraint surfaces. The update rule in equation (24) must therefore be chosen prudently so that the iterate is able to escape local minima if need be to avoid stagnation.

The simplest IPA is the error reduction (ER) algorithm (Fienup, 1982) in which the ith iterate is updated according to the rule

$$\mathbf{x}^{(i+1)} = P_S P_M \mathbf{x}^{(i)}. \tag{25}$$

The ER algorithm moves the iterate steadily towards a fixed point but is unable to escape and explore other regions of the search space if that fixed point turns out not to be a solution. Alternatively, the difference map (DM) algorithm (Elser, 2003*a*) uses an update rule which is able to escape local minima and is given by

$$\mathbf{x}^{(i+1)} = \mathbf{x}^{(i)} + \beta(P_S R_M - P_M R_S)\mathbf{x}^{(i)}, \tag{26}$$

where $|\beta| \leq 1$ is a parameter of the algorithm that can be thought of as the step size of the update, and R_S and R_M are relaxed projections defined by

$$R_S\mathbf{x}^{(i)} = \left[(1+\gamma_S)P_S - \gamma_S\right]\mathbf{x}^{(i)}$$
$$R_M\mathbf{x}^{(i)} = \left[(1+\gamma_M)P_M - \gamma_M\right]\mathbf{x}^{(i)}.$$

The amount of relaxation for the two relaxed projections is controlled by the parameters γ_S and γ_M. It is usual to set $\gamma_S = -1/\beta$, $\gamma_M = 1/\beta$ as justified by Elser (2003*b*). If the iterate no longer changes when the DM algorithm is applied, a solution $\mathbf{x}^{(\rm sol)}$ that satisfies both constraints is obtained from the current iterate $\mathbf{x}^{(i)}$ by

$$\mathbf{x}^{(\rm sol)} = P_S R_M \mathbf{x}^{(i)} = P_M R_S \mathbf{x}^{(i)}. \tag{27}$$

Another useful update rule that is capable of escaping local minima is the relaxed averaged alternating reflections (RAAR) algorithm (Luke, 2005) which can be expressed as

$$\mathbf{x}^{(i+1)} = \beta(2P_S P_M - P_S + 1)\mathbf{x}^{(i)} + (1-2\beta)P_M\mathbf{x}^{(i)}, \tag{28}$$

where β is again a parameter of the algorithm.

3.2. Phase retrieval from averaged finite crystal intensities

Our shape transform phasing problem at hand is to reconstruct the sets of functions $\{f_k(\mathbf{r})\}$ and $\{C_{kl}(\mathbf{q})\}$ for k and l ranging from 1 to K, given the averaged intensity function $I(\mathbf{q})$ defined by equation (14). The asymmetric unit $f(\mathbf{r})$ that we ultimately desire can be obtained from any one of the functions in $\{f_k(\mathbf{r})\}$ once a solution is found. The iterate in the IPA can therefore be represented as a real vector that contains the combined sets of samples in the real and imaginary parts of $\{f_k(\mathbf{r})\}$ and $\{C_{kl}(\mathbf{q})\}$. The length of this vector determines the dimension of the search space, D, which in turn corresponds to the amount of computer memory needed to store all of the variables in the problem. Here we provide an estimate for D and hence the memory requirement of our algorithm.

If we have N discrete samples in $\mathbf{q}$, we will also have N discrete samples in $\mathbf{r}$ since these two spaces are related by a discrete Fourier transform. In order to count the total number of independent samples in $\{C_{kl}(\mathbf{q})\}$, we introduce the sampling factor s that determines the number of samples between reciprocal-lattice points (Bragg reflections), which we assume in this analysis to be the same in all three dimensions. A sampling factor of $s = 1$ corresponds to the usual situation in crystallography in which there are no intensity samples between Bragg reflections, a sampling factor of $s = 2$ doubles the sampling along each direction in reciprocal space, and so on. Assuming a cubic array, the total number of samples N is then related to s by $N = (sL)^3$ where L is the number of resolution elements of the molecular density in each dimension, *i.e.* the reconstructed density of the molecule will be in an array of $L \times L \times L$ voxels.

Neglecting knowledge of the object support, non-crystallographic symmetry or other such parameter reductions, there are in total $K \times 2N = 2KN$ samples in the set $\{f_k(\mathbf{r})\}$ when accounting for both the real and imaginary parts of the potentially complex scattering densities. The set $\{C_{kl}(\mathbf{q})\}$ has far fewer independent parameters than $K^2 \times 2N = 2K^2N$, because of the many relations developed in Section 2, *i.e.* $C_{kl}(\mathbf{q})$ is periodic and inversion symmetric with respect to $\mathbf{q}$ [equations (16) and (17)], and Hermitian with respect to the indices k, l [equation (18)].

Applying the property of periodicity of $C_{kl}(\mathbf{q})$, the number of independent $\mathbf{q}$ samples in the averaged shape transform is no greater than the number of samples contained in its periodic domain, *i.e.* the shape transform cell, which is equal to s^3. Taking into account centrosymmetry, the number of independent $\mathbf{q}$ samples in the shape transform cell is therefore approximately $s^3/2$ (approximate due to the discrete nature of the problem). Finally, at each $\mathbf{q}$, the complex matrix $\mathbf{C}(\mathbf{q})$ has a total of K^2 independent real parameters when accounting for Hermitian symmetry. Thus, the overall dimension of the search space is approximately equal to

$$\begin{aligned} D &\approx 2KN + K^2 s^3/2 \\ &= 2Ks^3(L^3 + K/4). \end{aligned} \tag{29}$$

Typically, L^3 is large compared with K (say $L = 64$, $K = 4$) so D scales roughly as $2KN = 2K(sL)^3$, meaning that the amount of computer memory taken up by the averaged shape transforms is negligible compared with the arrays needed to hold the set $\{f_k(\mathbf{r})\}$. Note that the above analysis does not determine the constraint ratio Ω (Elser & Millane, 2008), defined as the ratio of the number of independent known samples to the number of independent unknown parameters. This is because some of the samples involved in the counting above are not independent or are known to be zero given the support of $f_k(\mathbf{r})$. We provide a discussion of Ω in the context of our problem in Appendix *B*.

To summarize, the iterate in the IPA for our shape transform phasing formulation is a real vector of length approximately $2Ks^3(L^3 + K/4)$ containing the combined sets of samples in the real and imaginary parts of $\{f_k(\mathbf{r})\}$ and $\{C_{kl}(\mathbf{q})\}$ for k and l ranging from 1 to K. Having defined what the iterate is, we can now describe the projection operators that act on this iterate.

3.3. Reciprocal-space constraints and the projection operator P_M

The operator P_M acts on the iterate $\mathbf{x}$ defined in the previous section to generate an output, $P_M\mathbf{x}$, that satisfies the data constraint

$$I_{\rm data}(\mathbf{q}) = \sum_{k=1}^{K}\sum_{l=1}^{K} F_k^*(\mathbf{q})C_{kl}(\mathbf{q})F_l(\mathbf{q}). \tag{30}$$

A particular combination of operations that is able to make an iterate satisfy equation (30) can be summarized in the following three steps:

Step (i). The averaged shape transforms $\{C_{kl}(\mathbf{q})\}$ are updated via a least-squares procedure using the intensity data and the current estimate of the molecular transforms $\{F_k(\mathbf{q})\}$.

Step (ii). A positive semi-definite projection operation is applied to the averaged shape transforms obtained from step (i), which ensures that the intensity values calculated using $\{F_k(\mathbf{q})\}$ and $\{C_{kl}(\mathbf{q})\}$ are non-negative.

Step (iii). The molecular transforms $\{F_k(\mathbf{q})\}$ are updated given the intensity data and the new averaged shape transforms from step (ii) with an operation that corresponds to a projection onto a hyper-ellipsoid.

Note that although each of these steps is in fact a distance-minimizing operation, as will be shown next, the combination of them yielding P_M turns out not to be a distance-minimizing operator in general. The reason for this is that step (i) holds $\{F_k(\mathbf{q})\}$ constant while it updates $\{C_{kl}(\mathbf{q})\}$ and vice versa for step (iii). We would need an operation that updates both the F's and C's simultaneously in a distance-minimizing way for P_M to be strictly classified as a projection operator. However, in its current form, P_M does change the iterate such that it satisfies the intensity data, which is the desired constraint. P_M could therefore be referred to as a 'constraint-satisfaction operator'.

Next we describe these three steps in detail.

3.3.1. Step (i). Updating the averaged shape transforms $\{C_{kl}(\mathbf{q})\}$. Since the averaged shape transforms are translationally symmetric according to

$$C_{kl}(\mathbf{q} - \mathbf{g_h}) = C_{kl}(\mathbf{q}), \tag{31}$$

where $\mathbf{g_h}$ is a reciprocal-lattice vector indexed by $\mathbf{h}$, it is helpful to divide reciprocal-space vectors into two components: $\mathbf{q} = \mathbf{q_{hm}} = \mathbf{g_h} + \mathbf{q_m}$. Under this formulation, the index $\mathbf{h}$ specifies a shape transform cell and the index $\mathbf{m}$ refers to a specific point within that particular cell, as depicted in Fig. 4. Upon consideration of the translational symmetry $C_{kl}(\mathbf{q}) = C_{kl}(\mathbf{q_m})$, as evident from equation (31), we write the diffracted intensities as

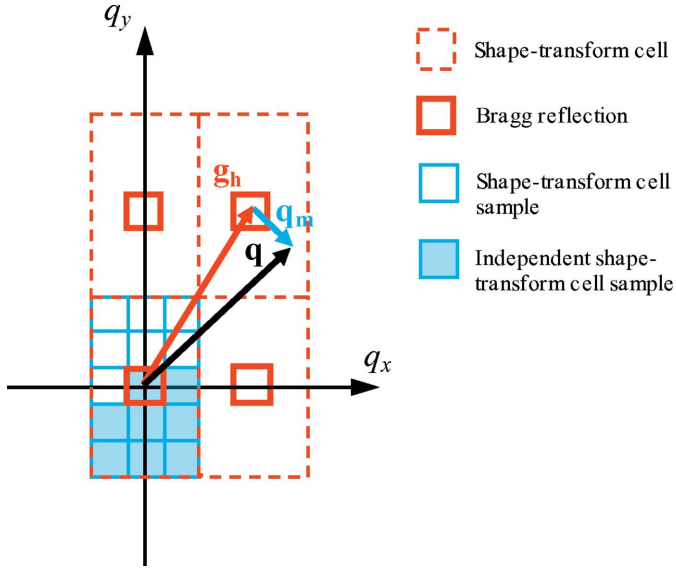

Figure 4
Explanation of the $\mathbf{q}$ vector indexing scheme in 2D reciprocal space. Red dashed boxes, indexed by $\mathbf{h}$, are the shape transform cells. Small blue squares, indexed by $\mathbf{m}$, are the samples within the shape transform cells. The thick-outlined small red squares are the Bragg reflections; thus each shape transform cell is associated with a Bragg reflection. Periodicity of the averaged shape transform $C_{kl}(\mathbf{q})$ implies the set of blue squares shown (both filled and empty) will be the same in each of the red dashed boxes. Inversion symmetry of the shape transform cells means the filled blue squares are the only unique samples within the cell. Note the entire diagram repeats to infinity in the two $\mathbf{q}$-space directions in principle.

$$I(\mathbf{q}) = I(\mathbf{g_h} + \mathbf{q_m}) = \sum_{k=1}^{K}\sum_{l=1}^{K} F_k^*(\mathbf{g_h} + \mathbf{q_m})C_{kl}(\mathbf{q_m})F_l(\mathbf{g_h} + \mathbf{q_m}). \tag{32}$$

Now consider gathering together samples of $I(\mathbf{q})$ and $F_k^*(\mathbf{q})F_l(\mathbf{q})$ at the $\mathbf{q}$ vectors with identical $C_{kl}(\mathbf{q})$. These samples form subsets of all samples within the functions $I(\mathbf{q})$ and $F_k^*(\mathbf{q})F_l(\mathbf{q})$. The subsets consist of all reciprocal-space positions $\mathbf{q}$ that have the same $\mathbf{m}$, and inversion-symmetry-related $-\mathbf{m}$, but different $\mathbf{h}$. Let there be a total of H such samples in a subset, indexed by h, and B subsets altogether, indexed by b. For the bth subset, equation (32) can be expressed in matrix form as

$$\mathbf{I}_b = \mathbf{Z}_b\mathbf{C}_b. \tag{33}$$

The term $\mathbf{I}_b$ is an $H \times 1$ column matrix containing the intensity samples $I(\mathbf{q_{hm}})$ and $I[\mathbf{q_{h(-m)}}]$, which we abbreviate as I_{bh} for compactness. The term $\mathbf{Z}_b$ is an $H \times K^2$ matrix consisting of the products $F_k^*(\mathbf{q_{hm}})F_l(\mathbf{q_{hm}})$ and $F_k^*[\mathbf{q_{h(-m)}}]F_l[(\mathbf{q_{h(-m)}}]$, which we abbreviate as $F_{kbh}^*F_{lbh}$. Finally, the term $\mathbf{C}_b$ is a $K^2 \times 1$ column matrix consisting of the samples $C_{kl}(\mathbf{q_m})$ which we abbreviate as C_{klb}.

Since there are many ways to form the matrices in equation (33), we look to an example in which there are only two molecular orientations, *i.e.* $K = 2$, to gain intuition. Multiplying out equation (32) and using the above notation gives

$$I_{bh} = |F_{1bh}|^2C_{11b} + |F_{2bh}|^2C_{22b} + F_{1bh}^*F_{2bh}C_{12b} + F_{1bh}F_{2bh}^*C_{21b}. \tag{34}$$

Note that since $C_{21}(\mathbf{q}) = C_{12}^*(\mathbf{q})$ we may rewrite equation (34) as

$$\begin{aligned} I_{bh} = {} & |F_{1bh}|^2C_{11b} + |F_{2bh}|^2C_{22b} + 2\mathrm{Re}(F_{1bh}^*F_{2bh})\mathrm{Re}(C_{12b}) \\ & - 2\mathrm{Im}(F_{1bh}^*F_{2bh})\mathrm{Im}(C_{12b}) \end{aligned} \tag{35}$$

so that the entries of the $\mathbf{Z}_b$ matrix and the $\mathbf{C}_b$ vector are all real. Stacking equation (35) up for all h gives the matrix equation $\mathbf{I}_b = \mathbf{Z}_b\mathbf{C}_b$ for this example:

$$\begin{bmatrix} I_{b1} \\ \vdots \\ I_{bH} \end{bmatrix} = \begin{bmatrix} |F_{1b1}|^2 & |F_{2b1}|^2 & 2\mathrm{Re}(F_{1b1}^*F_{2b1}) & -2\mathrm{Im}(F_{1b1}^*F_{2b1}) \\ & & \vdots & \\ |F_{1bH}|^2 & |F_{2bH}|^2 & 2\mathrm{Re}(F_{1bH}^*F_{2bH}) & -2\mathrm{Im}(F_{1bH}^*F_{2bH}) \end{bmatrix} \times \begin{bmatrix} C_{11b} \\ C_{22b} \\ \mathrm{Re}(C_{12b}) \\ \mathrm{Im}(C_{12b}) \end{bmatrix}. \tag{36}$$

Returning to the discussion of our general problem, there are in total B such matrix equations that can be formed using the current estimate of the averaged shape transforms $\{C_{kl}^{(i)}(\mathbf{q})\}$, giving $\mathbf{I}_b = \mathbf{Z}_b\mathbf{C}_b^{(i)}$. Each of these matrix equations can be inverted to obtain a new estimate of the averaged shape transform, denoted here by $\mathbf{C}_b'$, via

$$\mathbf{C}_b' = \mathbf{C}_b^{(i)} + \mathbf{Z}_b^+[\mathbf{I}_b - \mathbf{Z}_b\mathbf{C}_b^{(i)}], \tag{37}$$

where $\mathbf{Z}_b^+$ is the pseudo-inverse of $\mathbf{Z}_b$. The pseudo-inverse can be calculated by first forming the singular value decomposition of $\mathbf{Z}_b$, *i.e.* $\mathbf{Z}_b = \mathbf{U}_b\mathbf{\Sigma}_b\mathbf{V}_b^\dagger$ where $\mathbf{U}_b$ and $\mathbf{V}_b$ are unitary matrices of shape $H \times H$ and $K^2 \times K^2$, respectively, and $\mathbf{\Sigma}_b$ is the rectangular diagonal matrix of shape $H \times K^2$ containing all the singular values of $\mathbf{Z}_b$, denoted by σ_k, along the diagonal. The pseudo-inverse of $\mathbf{Z}_b$ is then given by

$$\mathbf{Z}_b^+ = \mathbf{V}_b\mathbf{\Sigma}_b^+\mathbf{U}_b^\dagger, \tag{38}$$

where $\mathbf{\Sigma}_b^+$ is the rectangular diagonal matrix containing the reciprocal of all the singular values of $\mathbf{Z}_b$, with entries corresponding to singular values less than some threshold ε set to zero, *i.e.*

$$\mathbf{\Sigma}_b^+ = \begin{cases} 1/\sigma_k & \sigma_k \geq \varepsilon \\ 0 & \sigma_k < \varepsilon \end{cases}. \tag{39}$$

Equation (37) is the least-squares solution to $\mathbf{C}_b$ that minimizes the distance between $\mathbf{C}_b^{(i)}$ and $\mathbf{C}_b'$ measured in terms of the 2-norm, defined for two arbitrary column matrices $\mathbf{A}$ and $\mathbf{B}$ as $||\mathbf{B} - \mathbf{A}||_2 = (\sum_i |\mathbf{B}_i - \mathbf{A}_i|^2)^{1/2}$. The derivation of equation (37) is detailed in Appendix *C*. Carrying out the least-squares estimate given by equation (37) for every b results in an updated estimate of the averaged shape transforms over all $\mathbf{q}$, denoted here by $C_{kl}'(\mathbf{q})$. Note the use of a prime in $C_{kl}'(\mathbf{q})$, which indicates that this temporary estimate will be further updated in the next step.

3.3.2. Step (ii). Enforcing positive semi-definiteness of $\{C_{kl}(\mathbf{q})\}$. The diffracted intensity calculated using the above intermediate estimate of the averaged shape transforms, $C_{kl}'(\mathbf{q})$, along with the current molecular transform estimates, $F_k^{(i)}(\mathbf{q})$, may produce negative intensity values, which are unphysical. More explicitly, for the estimate of the averaged shape transforms, $C_{kl}'(\mathbf{q})$, the expression

$$I'(\mathbf{q}) = \sum_{k=1}^{K}\sum_{l=1}^{K} F_k^{(i)*}(\mathbf{q})C_{kl}'(\mathbf{q})F_l^{(i)}(\mathbf{q}) \tag{40}$$

is not guaranteed to be greater than or equal to 0 for all $\mathbf{q}$. Equation (40) is a quadratic form and can be written in matrix form as was done in equation (20), giving

$$I'(\mathbf{q}) = \mathbf{F}^{(i)\dagger}(\mathbf{q})\mathbf{C}'(\mathbf{q})\mathbf{F}^{(i)}(\mathbf{q}). \tag{41}$$

Demanding $I'(\mathbf{q}) \geq 0$ for any $\mathbf{F}^{(i)}(\mathbf{q})$ implies the matrix $\mathbf{C}'(\mathbf{q})$ must be positive semi-definite (PSD). Thus, we seek an operation to ensure that $\mathbf{C}'(\mathbf{q})$ is PSD for every $\mathbf{q}$, which we explain below.

The projection operation that modifies an arbitrary matrix $\mathbf{A}$ to form a PSD matrix $\mathbf{B}$ while minimizing the Frobenius norm $||\mathbf{B} - \mathbf{A}||_\mathrm{F} = (\sum_i \sum_j |\mathbf{B}_{ij} - \mathbf{A}_{ij}|^2)^{1/2}$ is described by Higham (1988). We provide an alternative derivation of this operation in Appendix *D*. This projection operation consists of three steps: (i) eigen-decompose $\mathbf{A}$, (ii) set all the negative eigenvalues of $\mathbf{A}$ to zero, and (iii) eigen-recompose with the new set of non-negative eigenvalues.

In the context of our problem, first eigen-decompose $\mathbf{C}'(\mathbf{q})$ into the diagonal matrix $\mathbf{\Lambda}'(\mathbf{q})$ and unitary transform $\mathbf{U}(\mathbf{q})$ such that

$$\mathbf{C}'(\mathbf{q}) = \mathbf{U}(\mathbf{q})\mathbf{\Lambda}'(\mathbf{q})\mathbf{U}^{\dagger}(\mathbf{q}). \tag{42}$$

A new diagonal matrix $\mathbf{\Lambda}(\mathbf{q})$ is then formed by setting the negative entries of $\mathbf{\Lambda}'(\mathbf{q})$ to zero and leaving the non-negative entries unchanged, *i.e.*

$$\lambda_k(\mathbf{q}) = \begin{cases} \lambda'_k(\mathbf{q}) & \lambda'_k(\mathbf{q}) \geq 0 \\ 0 & \lambda'_k(\mathbf{q}) < 0 \end{cases}, \tag{43}$$

where $\lambda_k(\mathbf{q})$ and $\lambda'_k(\mathbf{q})$ are the kth eigenvalues, and hence kth diagonal entries, in the $K \times K$ diagonal matrices $\mathbf{\Lambda}(\mathbf{q})$ and $\mathbf{\Lambda}'(\mathbf{q})$, respectively. Finally, we eigen-recompose to form the new $\mathbf{C}^{(i+1)}(\mathbf{q})$ that is PSD via

$$\mathbf{C}^{(i+1)}(\mathbf{q}) = \mathbf{U}(\mathbf{q})\mathbf{\Lambda}(\mathbf{q})\mathbf{U}^{\dagger}(\mathbf{q}). \tag{44}$$

The updated averaged shape transforms $C_{kl}^{(i+1)}(\mathbf{q})$ are then the (k, l)th entries of the matrix $\mathbf{C}^{(i+1)}(\mathbf{q})$.

3.3.3. Step (iii). Updating $\{F_k(\mathbf{q})\}$. We would like to now make the smallest possible change to the current estimate of the molecular transforms, $\{F_k^{(i)}(\mathbf{q})\}$, such that the updated versions $\{F_k^{(i+1)}(\mathbf{q})\}$ satisfy

$$I_{\text{data}}(\mathbf{q}) = \sum_{k=1}^{K}\sum_{l=1}^{K} F_k^{(i+1)*}(\mathbf{q})C_{kl}^{(i+1)}(\mathbf{q})F_l^{(i+1)}(\mathbf{q}). \tag{45}$$

First let us investigate the geometry of the constraint equation (45). Writing down the matrix form of equation (45) yields

$$I_{\text{data}}(\mathbf{q}) = \mathbf{F}^{(i+1)\dagger}(\mathbf{q})\mathbf{C}^{(i+1)}(\mathbf{q})\mathbf{F}^{(i+1)}(\mathbf{q}). \tag{46}$$

Inserting the eigen-decomposition of $\mathbf{C}^{(i+1)}(\mathbf{q})$ from equation (44) gives

$$I_{\text{data}}(\mathbf{q}) = \mathbf{F}^{(i+1)\dagger}(\mathbf{q})\mathbf{U}(\mathbf{q})\mathbf{\Lambda}(\mathbf{q})\mathbf{U}^{\dagger}(\mathbf{q})\mathbf{F}^{(i+1)}(\mathbf{q}) \tag{47}$$

which can be written as

$$I_{\text{data}}(\mathbf{q}) = \mathbf{F}'^{(i+1)\dagger}(\mathbf{q})\mathbf{\Lambda}(\mathbf{q})\mathbf{F}'^{(i+1)}(\mathbf{q}), \tag{48}$$

where we have introduced the primed variable

$$\mathbf{F}'^{(i+1)}(\mathbf{q}) = \mathbf{U}^{\dagger}(\mathbf{q})\mathbf{F}^{(i+1)}(\mathbf{q}). \tag{49}$$

Expanding the matrix product, equation (48) can be written as

$$I_{\text{data}}(\mathbf{q}) = \sum_{k=1}^{K} \lambda_k(\mathbf{q})|F_k'^{(i+1)}(\mathbf{q})|^2, \tag{50}$$

where $\lambda_k(\mathbf{q})$ is the kth eigenvalue of $\mathbf{C}^{(i+1)}(\mathbf{q})$. Since $F_k'^{(i+1)}(\mathbf{q})$ is complex and the $\lambda_k(\mathbf{q})$'s are not necessarily the same, equation (50) is an equation of a hyper-ellipsoid in $2K$-dimensional space.

To form the projection onto the constraint equation (50) from the initial starting point $\mathbf{F}^{(i)}(\mathbf{q})$, we first apply the same unitary transformation on the current estimate of the molecular transform, yielding $\mathbf{F}'^{(i)}(\mathbf{q}) = \mathbf{U}^{\dagger}(\mathbf{q})\mathbf{F}^{(i)}(\mathbf{q})$. We then seek the minimum change to $\mathbf{F}'^{(i)}(\mathbf{q})$ such that it satisfies equation (50). The distance-minimizing property of such an operation is carried over from $\mathbf{F}'$ to $\mathbf{F}$ as Euclidean distances are preserved under unitary transformations. Using the method of Lagrange multipliers, we show in Appendix *E* that the projection onto the multi-dimensional ellipsoid described by equation (50) is given by

$$F_k'^{(i+1)}(\mathbf{q}) = \frac{F_k'^{(i)}(\mathbf{q})}{1 + \beta(\mathbf{q})\lambda_k(\mathbf{q})} \tag{51}$$

where $\beta(\mathbf{q})$ is the Lagrange multiplier which is obtained by solving the equation

$$I_{\text{data}}(\mathbf{q}) = \sum_{k=1}^{K} \frac{\lambda_k(\mathbf{q})|F_k'^{(i)}(\mathbf{q})|^2}{[1 + \beta(\mathbf{q})\lambda_k(\mathbf{q})]^2}. \tag{52}$$

Equation (52) can be solved for $\beta(\mathbf{q})$ by rearranging it into a polynomial of degree $2K$ and using a numerical polynomial solver to obtain the roots.

In that case, there are up to $2K$ possible solutions for $\beta(\mathbf{q})$. In order to find the $\beta(\mathbf{q})$ that minimizes the distance between $\mathbf{F}'^{(i+1)}(\mathbf{q})$ and $\mathbf{F}'^{(i)}(\mathbf{q})$, each obtained root is substituted into equation (51) to form a candidate solution $\mathbf{F}'^{(i+1)}(\mathbf{q})$ and for each of those candidates the distance $||\mathbf{F}'^{(i+1)}(\mathbf{q}) - \mathbf{F}'^{(i)}(\mathbf{q})||_2$ is calculated. The $\mathbf{F}'^{(i+1)}(\mathbf{q})$ that gives the minimum distance is then the projection onto the constraint equation (50). For K large (greater than about 6), massive differences in the magnitudes of the polynomial coefficients can cause numerical problems and prevent accurate determination of the roots via the rearrangement of equation (52) into a degree $2K$ polynomial. In those cases it is better to work with equation (52) directly and solve for $\beta(\mathbf{q})$ via, for example, the bisection method as detailed by Morgan *et al.* (2019). We also adopt this approach here but use instead the bisection-bounded Newton–Raphson method where the root search is started in the state of Newton–Raphson for each iteration, only reverting to the bisection method for iterations where the new estimate of the root falls outside the bound provided for bisection. The bounds are updated by the estimate of the root obtained from the previous iteration as the root-finding algorithm proceeds. The initial bound is given by $(-1/\lambda_{\max}, +\infty)$ where $\lambda_{\max}$ is the largest eigenvalue of $\mathbf{C}^{(i+1)}(\mathbf{q})$. This bound is a result of the observation that the distance-minimizing solution that gives the projection of a point onto a hyper-ellipsoid must lie within the same quadrant as that point, *i.e.* the components of the starting point should have the same sign as the components of the projected point. In terms of equation (51), this statement says that $F_k'^{(i+1)}(\mathbf{q})$ must have the same sign as $F_k'^{(i)}(\mathbf{q})$, which means $1 + \beta(\mathbf{q})\lambda_k(\mathbf{q})$ must be greater than zero, and hence $\beta(\mathbf{q}) > -1/\lambda_{\max}$, giving us the initial bound.

After the Lagrange multiplier $\beta(\mathbf{q})$ for the distance-minimizing solution has been determined, it can be substituted into equation (51) to yield the required $\mathbf{F}'^{(i+1)}(\mathbf{q})$ as before. The geometric interpretation of equation (51) is that $\beta(\mathbf{q}) > 0$ implies the starting point is outside the hyper-ellipsoid and we are projecting inwards by making $F_k'^{(i)}(\mathbf{q})$ smaller, $\beta(\mathbf{q}) < 0$ implies the starting point is inside the hyper-ellipsoid and we are projecting outwards by making $F_k'^{(i)}(\mathbf{q})$ larger, $\beta(\mathbf{q}) = 0$ implies the starting point is already on the hyper-ellipsoid and we do not need to do anything, as evident by equation (51) where $F_k'^{(i+1)}(\mathbf{q}) = F_k'^{(i)}(\mathbf{q})$ when $\beta(\mathbf{q}) = 0$. Projections onto

ellipsoids have been considered by Stark & Yang (1998), Borwein *et al.* (2018), Morgan *et al.* (2019) and projections onto more general constraint surfaces have been outlined by Elser (2017).

Once the required $\mathbf{F}'^{(i+1)}(\mathbf{q})$ has been determined, the new estimates of the molecular transform are finally obtained by applying the inverse transformation

$$\mathbf{F}^{(i+1)}(\mathbf{q}) = \mathbf{U}(\mathbf{q})\mathbf{F}'^{(i+1)}(\mathbf{q}). \tag{53}$$

3.3.4. Summary of the P_M operator. To summarize, the three steps of the P_M operator results in the update

$$P_M\mathbf{x}^{(i)} = P_M\{F_k^{(i)}(\mathbf{q}), C_{kl}^{(i)}(\mathbf{q})\} = \{F_k^{(i+1)}(\mathbf{q}), C_{kl}^{(i+1)}(\mathbf{q})\} \tag{54}$$

such that $\{C_{kl}^{(i+1)}(\mathbf{q})\}$ has the correct periodicity, the matrix $\mathbf{C}^{(i+1)}(\mathbf{q})$ is PSD, and along with the updated molecular transforms $\{F_k^{(i+1)}(\mathbf{q})\}$, the intensity data constraint equation (45) is satisfied.

Note that, as mentioned at the start of this section (Section 3.3), P_M is strictly not a projection since it holds $\{F_k(\mathbf{q})\}$ constant while it updates $\{C_{kl}(\mathbf{q})\}$ and vice versa. We would need an operation that updates both the F's and C's simultaneously in a distance-minimizing way for P_M to be strictly classified as a projection operator. However, in its current form, P_M does change the iterate such that it satisfies the intensity data and each of the steps within P_M are in fact distance-minimizing individually.

A further note on the use of P_M is that, under certain circumstances, a degeneracy exists that prevents the unique retrieval of $\{C_{kl}(\mathbf{q})\}$. In 2D, this degeneracy arises if any molecules with real density values are related by a 180° rotation, *e.g.* in the $P2$ space group, the Fourier transform of those molecules will have the same intensity due to Friedel symmetry. The two coinciding symmetries mean that two of the rows in the matrix $\mathbf{Z}_b$ from equation (33) are identical and therefore the outer product $\mathbf{Z}_b^{\mathrm{T}}\mathbf{Z}_b$ becomes non-invertible. This issue is handled by the pseudo-inverse $\mathbf{Z}_b^{+}$; however it has implications for the reconstruction problem as follows. Consider the $K = 2$ example in equation (34). If $|F_{1bh}|^2 = |F_{2bh}|^2$ then equation (35) can be rewritten as

$$\begin{aligned} I_{bh} = {} & |F_{1bh}|^2(C_{11b} + C_{22b}) + 2\mathrm{Re}(F_{1bh}^* F_{2bh})\mathrm{Re}(C_{12b}) \\ & - 2\mathrm{Im}(F_{1bh}^* F_{2bh})\mathrm{Im}(C_{12b}) \end{aligned} \tag{55}$$

which leads to

$$\begin{bmatrix} I_{b1} \\ \vdots \\ I_{bH} \end{bmatrix} = \begin{bmatrix} |F_{1b1}|^2 & 2\mathrm{Re}(F_{1b1}^* F_{2b1}) & -2\mathrm{Im}(F_{1b1}^* F_{2b1}) \\ & \vdots & \\ |F_{1bH}|^2 & 2\mathrm{Re}(F_{1bH}^* F_{2bH}) & -2\mathrm{Im}(F_{1bH}^* F_{2bH}) \end{bmatrix} \times \begin{bmatrix} C_{11b} + C_{22b} \\ \mathrm{Re}(C_{12b}) \\ \mathrm{Im}(C_{12b}) \end{bmatrix}. \tag{56}$$

This example shows that we can only recover the sum of $C_{kk}(\mathbf{q})$ and $C_{ll}(\mathbf{q})$ at the $\mathbf{q}$ locations for which $|F_k(\mathbf{q})|^2 = |F_l(\mathbf{q})|^2$. In 3D this degeneracy arises when the molecules are related by inversion symmetry, which is rare for protein molecules. This degeneracy may also be possible when crystals are twinned. In that case, if we know the potential twinning operations then we can accommodate twinned intensity data sets by including the appropriate symmetry operators. However, we emphasize that this degeneracy affects only the recovery of $\{C_{kl}(\mathbf{q})\}$. If our objective is to recover $\{f_k(\mathbf{r})\}$, as in the case of shape transform phasing, this issue does not pose a problem.

3.4. Real-space constraints and projection operator P_S

The constraints that we use in real space are (i) known symmetry relations between $f_k(\mathbf{r})$ and $f_l(\mathbf{r})$ for all k, l, and (ii) the finite support for the asymmetric unit $f(\mathbf{r})$ that generates the support for the set of all $f_k(\mathbf{r})$. The real-space projection operator consists of sequentially applying the projection operators for these constraints and is implemented as follows. First, the inverse symmetry operations for each molecular density $f_k(\mathbf{r})$ are applied to re-map each molecule to the same position and orientation as the asymmetric unit $f(\mathbf{r})$. The set of K re-mapped $f_k(\mathbf{r})$ are then averaged, and the support constraint is applied to this average. We then rescale the averaged $f(\mathbf{r})$ such that the root-mean-squared value of its density is 1. This normalization procedure is useful because the intensity data constraint equation (30) cannot determine the absolute scale of the molecular transforms without prior knowledge of the absolute scale of the averaged shape transforms. By fixing the scale of $f_k(\mathbf{r})$ at each iteration, we avoid potential issues such as numerical overflow and this also aids the convergence of the algorithm by preventing drift in the overall scale. Finally, we map the resulting averaged asymmetric unit density back to the kth position by applying the kth set of symmetry operations.

The above description may be given notationally by

$$P_S f_k(\mathbf{r}) = \mathcal{L}_k\, P_{\mathrm{scale}}\, s(\mathbf{r}) \frac{1}{K}\sum_{k=1}^{K} \mathcal{L}_k^{-1} f_k(\mathbf{r}), \tag{57}$$

where the forward and inverse linear transformations $\mathcal{L}_k$ and $\mathcal{L}_k^{-1}$ are defined by equations (1) and (2), $s(\mathbf{r})$ is the binary support function for $f(\mathbf{r})$ defined by equation (21), and

$$P_{\mathrm{scale}} f(\mathbf{r}) = \frac{f(\mathbf{r})}{\left[\sum_{\mathbf{r}} |f(\mathbf{r})|^2\right]^{1/2}}. \tag{58}$$

3.5. Summary of constraints

Altogether, the constraints that we have are: averaged diffracted intensity data $I_{\mathrm{data}}(\mathbf{q})$; support for $f(\mathbf{r})$; real-space symmetry between $\{f_k(\mathbf{r})\}$; $\{C_{kl}(\mathbf{q})\}$ are periodic; $\{C_{kl}(\mathbf{q})\}$ are centrosymmetric; the matrices $\mathbf{C}(\mathbf{q})$ formed from $\{C_{kl}(\mathbf{q})\}$ are PSD.

A flow diagram illustrating the step-by-step procedures within the operators P_S and P_M is shown in Fig. 5. The inputs and outputs of the two operators are connected in Fig. 5 in the form of the ER algorithm.

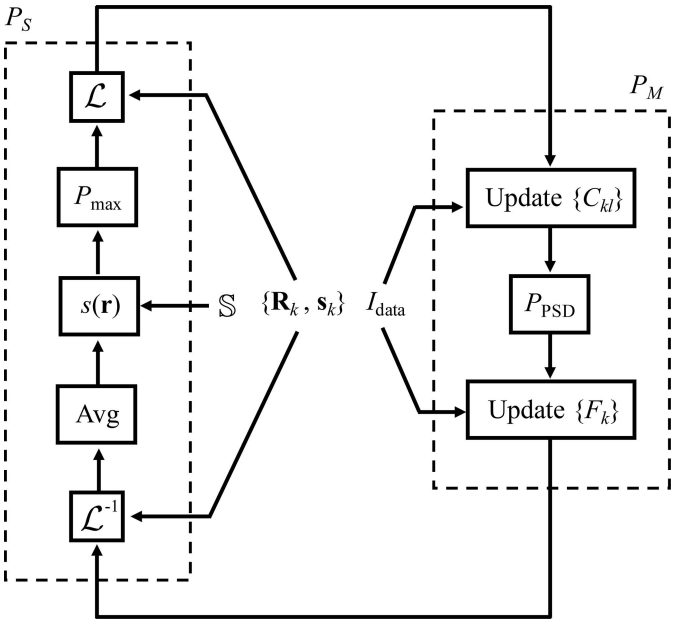

Figure 5
The steps of the projection operators and how they are combined to form the ER algorithm. The dashed boxes encapsulate the step-by-step recipe for each of the projections and the quantities $\mathbb{S}$, $\{\mathbf{R}_k, \mathbf{s}_k\}$ and I_{data} are the ingredients needed for the recipe. P_{PSD} is the positive semi-definite projection as outlined in Section 3.3.2.

4. Simulations

We conducted two sets of simulations to test the above algorithm: one for a synthetic image in 2D and the other for two protein molecules in 3D.

4.1. 2D simulation

The algorithm was first tested in 2D. A synthetic data set was constructed consisting of an ensemble of finite 2D crystals. The capital letter 'P' in bold Times New Roman font was selected as the support of the molecule. The scattering density of the molecule was chosen to be the Kodak test image 'kodim23' featuring two parrots. This was obtained by multiplying a binary letter-P mask with the kodim23 image that was resized to be of the same shape. The symmetry operation was chosen to be a reflection. There are thus two symmetry partners ($K = 2$), 'P' and mirrored 'P'.

The crystals were generated by defining two regions: (i) an inner region for the body of the crystal, (ii) an outer region on the perimeter of the inner region which constitutes the edge. The inner region is rectangular with its width and height randomly chosen from a uniform distribution. The outer region is defined to be a shell around the inner region with a width of one unit-cell lattice spacing away from the inner region. The probability of a molecule occupying a lattice point within the inner region is 1. The probability of a molecule occupying a lattice point within the outer region is 0.5.

Fig. 6 shows two example crystals and their diffracted intensity. The diffracted intensity was calculated using the discrete Fourier transform with five samples between each Bragg reflection, *i.e.* $s = 6$. The last row of Fig. 6 shows the result of averaging the intensities for 100 crystals and the behavior of a convergence metric, $\Delta\langle I_n(\mathbf{q})\rangle_n$. The convergence metric is defined as the difference between the averaged diffracted intensity from an ensemble of N crystals and that from the previous $N-1$ crystals summed over all $\mathbf{q}$, normalized to the intensity of the first crystal,

$$\begin{aligned}\Delta\langle I_n(\mathbf{q})\rangle_n &= \sum_{\mathbf{q}}\left[\frac{1}{N}\sum_{n=1}^{N} I_n(\mathbf{q}) - \frac{1}{N-1}\sum_{n=1}^{N-1} I_n(\mathbf{q})\right] \Big/ \sum_{\mathbf{q}} I_1(\mathbf{q}) \\ &= \sum_{\mathbf{q}}\left[\frac{1}{N} I_N(\mathbf{q}) - \frac{1}{N(N-1)}\sum_{n=1}^{N-1} I_n(\mathbf{q})\right] \Big/ \sum_{\mathbf{q}} I_1(\mathbf{q}).\end{aligned} \tag{59}$$

As can be seen from the last row of Fig. 6, the averaged intensity does not change much after the intensity from a few tens of crystals has been summed.

Iterative phase retrieval was carried out as described in Section 3. The correct support of the molecule was assumed to be known (the letter P). The positivity constraint was not applied. A periodic cycling of IPAs composed of 80 iterations of ER and 20 iterations of DM with $\beta = 0.6$, with the cycle being initiated in the ER state, was empirically found to work. The IPA was started such that the initial iterate, $\mathbf{x}^{(0)}$, had uniformly random sample values between 0 and 1 for both the sets of functions $\{f_k^{(0)}(\mathbf{r})\}$ and $\{C_{kl}^{(0)}(\mathbf{q})\}$.

Convergence of the entire iterative procedure was measured by the normalized root-mean-squared (NRMS) error, $E_I^{(i)}$, between $I_{\text{data}}(\mathbf{q})$ and the diffracted intensity $I^{(i)}(\mathbf{q})$ computed from the estimates $\{f_k^{(i)}(\mathbf{r})\}$ and $\{C_{kl}^{(i)}(\mathbf{q})\}$ via equation (14) at the ith iteration, *i.e.*

$$E_I^{(i)} = \left\{\frac{\sum_{\mathbf{q}}[I^{(i)}(\mathbf{q}) - I_{\text{data}}(\mathbf{q})]^2}{\sum_{\mathbf{q}} I_{\text{data}}^2(\mathbf{q})}\right\}^{1/2}. \tag{60}$$

The final reconstruction is obtained by taking the iterate at the iteration where $E_I^{(i)}$ is the minimum within the maximum number of iterations.

The quality of the reconstruction was measured by the NRMS error, $E_f^{(i)}$, between the true molecular density $f(\mathbf{r})$ and the ith estimate of the density, $f^{(i)}(\mathbf{r})$, *i.e.*

$$E_f^{(i)} = \left[\frac{\sum_{\mathbf{r}} |f^{(i)}(\mathbf{r}) - f(\mathbf{r})|^2}{\sum_{\mathbf{r}} |f(\mathbf{r})|^2}\right]^{1/2}, \tag{61}$$

and also by the NRMS error, $E_C^{(i)}$, between the true averaged shape transforms $\{C_{kl}(\mathbf{q})\}$ and the ith estimate $\{C_{kl}^{(i)}(\mathbf{q})\}$, *i.e.*

$$E_C^{(i)} = \left[\frac{\sum_k \sum_l \sum_{\mathbf{q}} |C_{kl}^{(i)}(\mathbf{q}) - C_{kl}(\mathbf{q})|^2}{\sum_k \sum_l \sum_{\mathbf{q}} |C_{kl}(\mathbf{q})|^2}\right]^{1/2}. \tag{62}$$

Fig. 7 shows the results from a successful run of the reconstruction. Only $C_{11}(\mathbf{q})$ and $C_{12}(\mathbf{q})$ (the real and imaginary parts) are shown.

4.2. 3D simulations

The proposed algorithm was tested in 3D with simulated diffraction from two different protein molecules that

crystallize with different numbers of molecular orientations (different values of K). The first is the Photosystem II (PSII) protein molecule with Protein Data Bank (PDB) entry 3wu2 (Umena *et al.*, 2011). The crystalline form of this protein consists of a single molecule (the asymmetric unit) in four different orientations ($K = 4$) with space group $P2_12_12_1$. The second molecule tested was the *Trypanosoma brucei* procathepsin B (CatB) protein molecule with PDB entry 4hwy (Redecke *et al.*, 2013). The crystalline form of this protein consists of a single molecule (the asymmetric unit) in eight different orientations ($K = 8$) with space group $P4_22_12$.

The electron density of the molecule was generated by first initializing a 3D array consisting of voxels at a specified resolution in real space; then, ignoring all the hydrogen atoms, each non-hydrogen atom is modeled as a Gaussian in real space scaled such that the integral of the Gaussian is equal to the number of electrons in the atom with a fixed width of one standard deviation equal to half an Å. The electron density was then obtained by summing all the Gaussians. We worked in the crystal basis for the entire simulation to avoid any interpolation or sampling issues when performing translation/rotation symmetry operations; our symmetry operators effectively consist of permutation matrices. The simulation results from the PSII protein are described first, followed by the results from the CatB molecule.

A total of 100 finite edgy crystals of the PSII protein are generated using the same edgy construction approach as the 2D simulation described in Section 4.1, with the inner and outer regions being bounded by 3D rectangular cuboids instead of 2D rectangles. The maximum size of the crystal for this particular simulation is $4 \times 4 \times 4$ full unit cells. Projection view of two example crystals from the ensemble is shown in Fig. 8. The far-field diffraction at a resolution of 10 Å was calculated with the discrete Fourier transform. The diffracted intensity had three samples between each Bragg reflection, *i.e.* $s = 4$. The calculated intensity was averaged to form the input averaged diffracted intensity data.

Iterative phase retrieval was carried out as described in Section 3. The correct support of the molecule was assumed to be known. The positivity constraint was not applied. A periodic cycling of IPAs composed of 60 iterations of ER and 40 iterations of DM with $\beta = 0.7$, with the cycle being initiated in the ER state, was empirically found to work. The initial iterate, $\mathbf{x}^{(0)}$, had uniformly randomly sampled values between 0 and 1 for both the sets of functions $\{f_k^{(0)}(\mathbf{r})\}$ and $\{C_{kl}^{(0)}(\mathbf{q})\}$. Convergence and quality of the entire iterative procedure

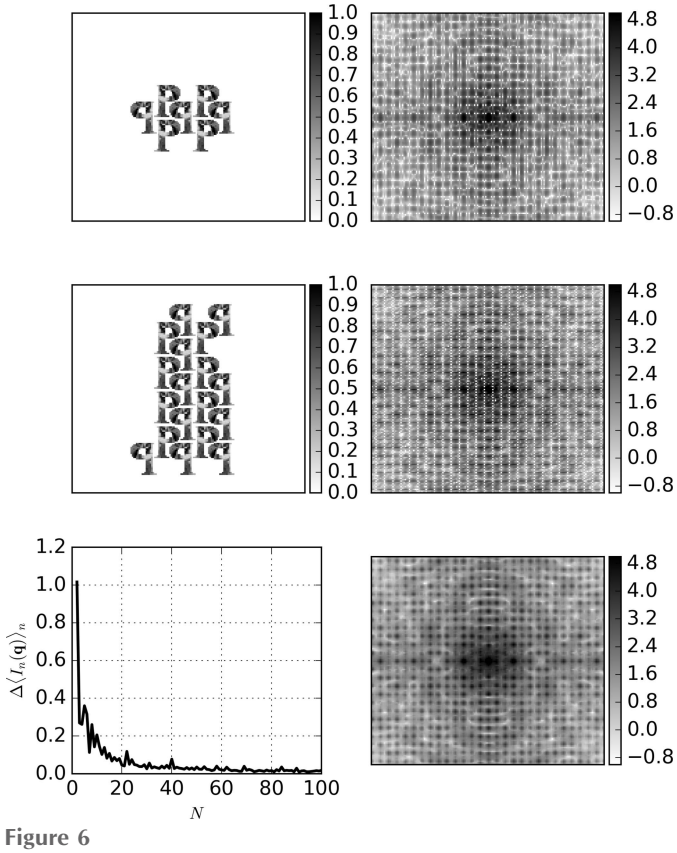

Figure 6
Example 2D crystals generated are shown in the left column. The right column shows their corresponding diffracted intensities on a log scale. The last row on the left shows the change in the averaged intensity as more diffracted intensities from different crystals are averaged, and on the right shows the final averaged intensity. The box that both the crystals and the diffracted intensities are shown in is the extent of the entire computational volume of the simulation.

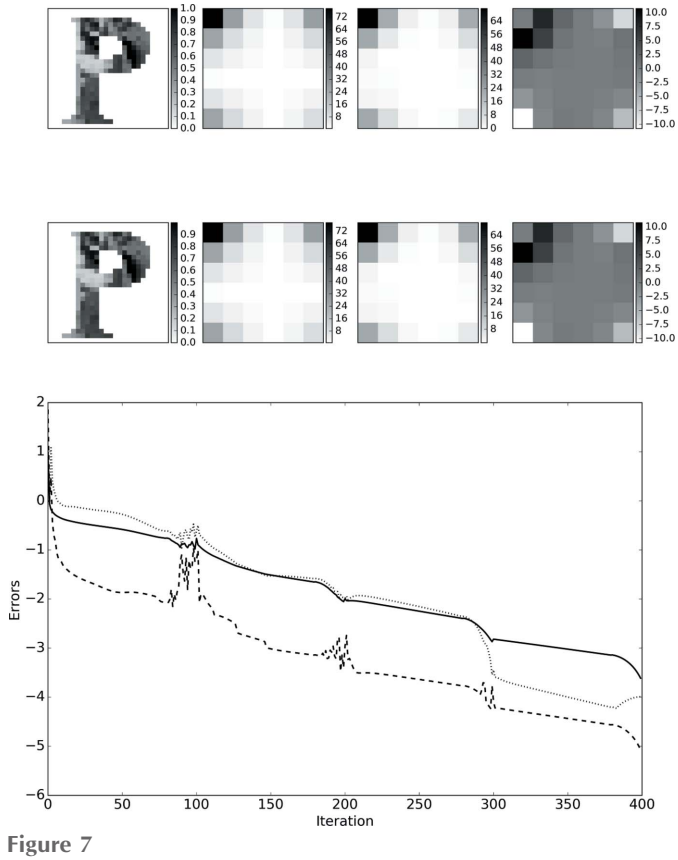

Figure 7
The top row shows the ground truth and the second row shows the best reconstruction as gauged by E_I. (Column 1) Real-space density of the molecule, (Column 2) $C_{11}(\mathbf{q})$, (Column 3) Re$[C_{12}(\mathbf{q})]$, (Column 4) Im$[C_{12}(\mathbf{q})]$. Only one period of the C_{kl} functions is shown (the shape transform cell). The bottom plot shows the reconstruction errors E_f (solid), E_C (dotted) and E_I (dashed) on a log scale as the algorithm proceeds.

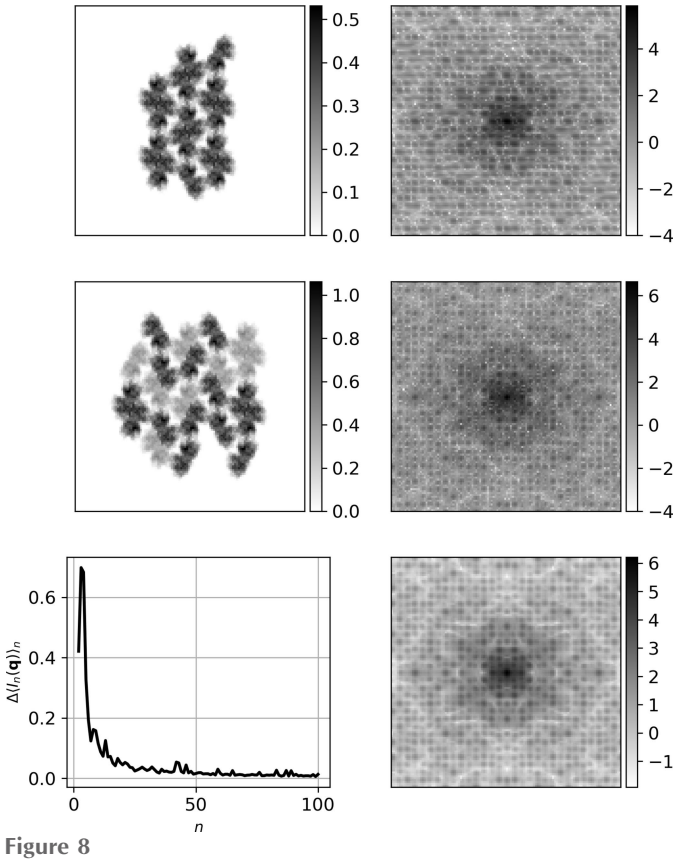

Figure 8
Projection views of two example crystals from the PSII molecule displayed in the crystal basis are shown in the left column. The right column shows one central slice of their corresponding 3D diffracted intensities on a log scale. The last row on the left shows the change in the averaged intensity as more diffracted intensities from different crystals are averaged, and on the right shows the same central slice of the final averaged 3D intensity. The box that both the crystals and the diffracted intensities are shown in is the extent of the computational volume of the simulation in two of the three directions.

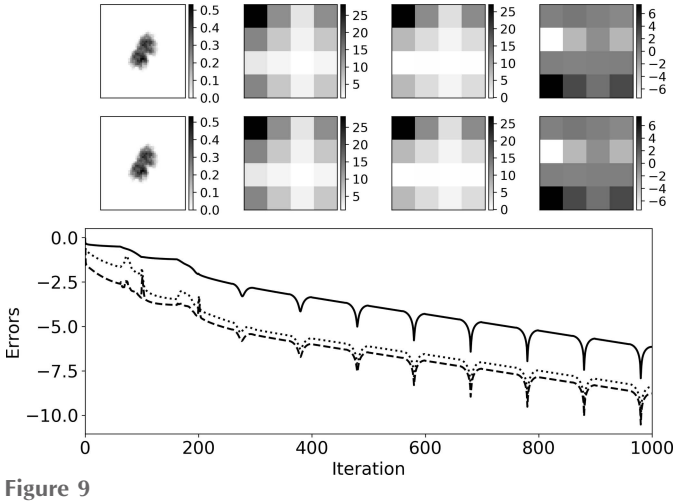

Figure 9
The top row shows the ground truth molecule and the second row shows the best reconstruction as gauged by E_I. (Column 1) Projected view of the molecule, (Column 2) $C_{11}(\mathbf{q})$, (Column 3) Re$[C_{12}(\mathbf{q})]$, (Column 4) Im$[C_{12}(\mathbf{q})]$. Only one slice of one period of the 3D C_{kl} functions is shown (the shape transform cell). The bottom plot shows the reconstruction errors E_f (solid), E_C (dotted) and E_I (dashed) on a log scale as the algorithm proceeds.

were again measured by the NRMS errors, E_I, E_f and E_C. Fig. 9 shows the results from a successful run of the reconstruction. The final reconstruction is obtained by taking the iterate at the iteration where E_I is the minimum. Only one slice from the 3D shape transform cell of two $C_{kl}(\mathbf{q})$ functions, $C_{11}(\mathbf{q})$ and $C_{12}(\mathbf{q})$, is shown as there are in total ten different $C_{kl}(\mathbf{q})$ functions.

The second protein molecule tested was CatB. A total of 100 finite edgy crystals of the CatB protein are generated using the same construction as described in Section 4.1, again with the inner and outer regions being bounded by 3D rectangular cuboids instead of 2D rectangles. The maximum size of the crystal for this particular simulation is $4 \times 4 \times 4$ full unit cells. Projection view of two example crystals from the ensemble is shown in Fig. 10. The far-field diffraction at a resolution of 4 Å was calculated with the discrete Fourier transform. The diffracted intensity had three samples between each Bragg reflection, *i.e.* $s = 4$. The calculated intensity was averaged to form the input averaged diffracted intensity data.

Iterative phase retrieval was carried out as described in Section 3. The correct support of the molecule was assumed to be known. The positivity constraint was not applied. A periodic cycling of IPAs composed of 300 iterations of ER and 100 iterations of RAAR with $\beta = 0.7$, with the cycle being initiated in the ER state, was empirically found to work. The initial iterate, $\mathbf{x}^{(0)}$, had uniformly randomly sampled values between 0 and 1 for both the sets of functions $\{f_k^{(0)}(\mathbf{r})\}$ and $\{C_{kl}^{(0)}(\mathbf{q})\}$. Convergence and quality of the entire iterative procedure were again measured by the NRMS errors, E_I, E_f and E_C. Fig. 11 shows the results from a successful run of the reconstruction. The final reconstruction is obtained by taking the iterate at the iteration where E_I is the minimum. Only one slice from the 3D shape transform cell of two $C_{kl}(\mathbf{q})$ functions, $C_{11}(\mathbf{q})$ and $C_{12}(\mathbf{q})$, is shown as there are in total 36 different $C_{kl}(\mathbf{q})$ functions.

4.3. 3D simulations with noise

The simulations in Section 4.2 are repeated with the addition of Poisson noise in the diffracted intensity and the simulated merging of a finite number of 2D diffraction slices in 3D reciprocal space. Edgy crystals of PSII and CatB, and their 3D diffracted intensities, are calculated with the same procedure and parameters as described in Section 4.2. The effect of merging 2D diffraction patterns was modeled by first generating a unit vector centered at the origin of reciprocal space with a uniformly randomly sampled orientation. This unit vector is taken to be the unit normal of a plane passing through the reciprocal-space origin and the set of all voxels that the plane intersects in the 3D diffraction volume is taken as the 2D diffracted intensity pattern measured from a single X-ray pulse diffracting from the finite edgy crystal. Poisson noise is then added to the intensity values at those voxels intersected by the plane. The resulting noisy 2D pattern is merged (averaged) into a 3D volume and the procedure is repeated with a newly generated edgy crystal. The final averaged diffracted intensity can be written as

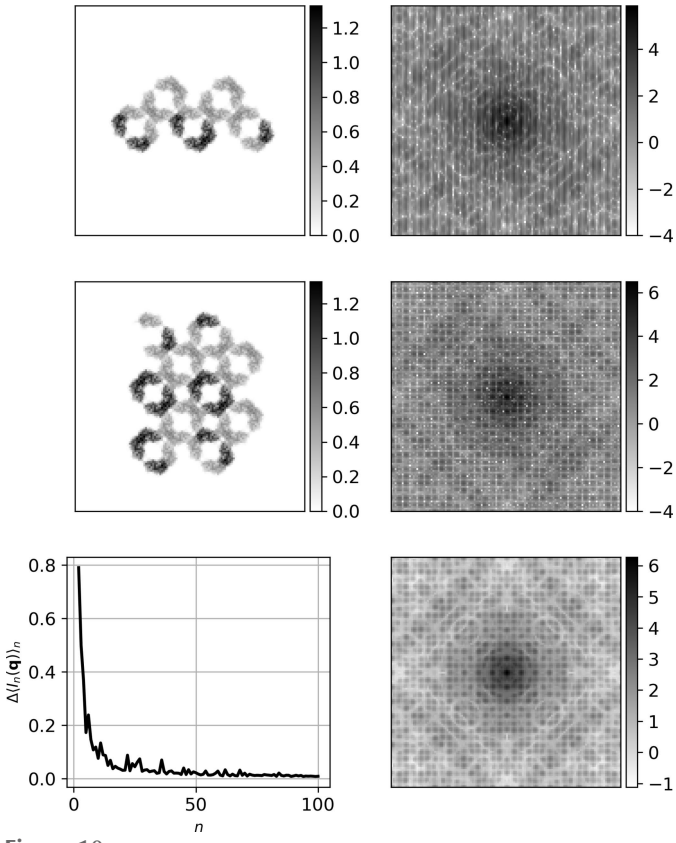

Figure 10
Projection views of two example crystals from the CatB molecule displayed in the crystal basis are shown in the left column. The right column shows one central slice of their corresponding 3D diffracted intensities on a log scale. The last row on the left shows the change in the averaged intensity as more diffracted intensities from different crystals are averaged, and on the right shows the same central slice of the final averaged 3D intensity. The box that both the crystals and the diffracted intensities are shown in is the extent of the computational volume of the simulation in two of the three directions.

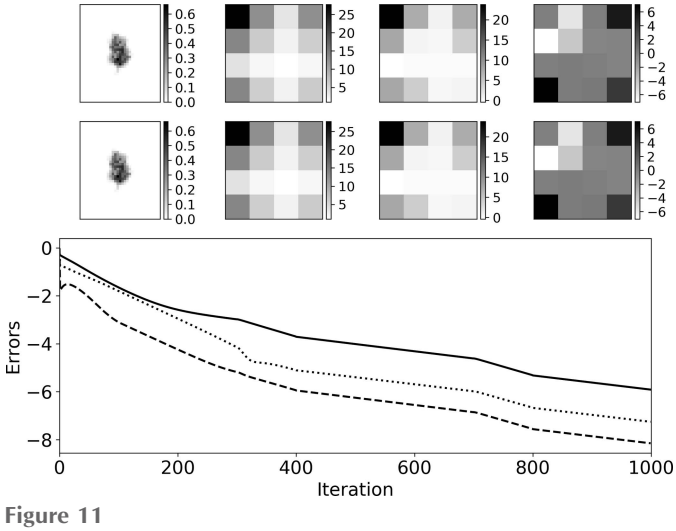

Figure 11
The top row shows the ground truth molecule and the second row shows the best reconstruction as gauged by E_I. (Column 1) Projected view of the molecule, (Column 2) $C_{11}(\mathbf{q})$, (Column 3) Re$[C_{12}(\mathbf{q})]$, (Column 4) Im$[C_{12}(\mathbf{q})]$. Only one slice of one period of the 3D C_{kl} functions is shown (the shape transform cell). The bottom plot shows the reconstruction errors E_f (solid), E_C (dotted) and E_I (dashed) on a log scale as the algorithm proceeds.

$$I_{\text{noisy data}}(\mathbf{q}) = \left\langle \frac{1}{\eta}\text{Po}[\eta I_n(\mathbf{q})] \right\rangle_n , \tag{63}$$

where Po(x) is a function that returns a value drawn from a Poisson probability density function of mean x. The scale factor η is chosen to give a desired level of noise and the average is over the number of times the particular voxel in reciprocal space was sampled by the randomly oriented 2D diffraction plane. To summarize, our noise generation procedure is: (i) calculate the entire 3D diffracted intensity from an individual 3D crystal; (ii) take a single random 2D central slice from that 3D intensity; (iii) apply Poisson noise to that 2D slice; (iv) merge the noisy 2D slice into a 3D averaged diffracted intensity volume; (v) repeat step (i) with a different crystal.

The signal-to-noise ratio (SNR) is calculated as

$$\text{SNR} = \left\{ \frac{\sum_{\mathbf{q}} I^2_{\text{data}}(\mathbf{q})}{\sum_{\mathbf{q}} [I_{\text{data}}(\mathbf{q}) - I_{\text{noisy data}}(\mathbf{q})]^2} \right\}^{1/2} \tag{64}$$

where I_{data} is the noiseless averaged diffracted intensity, and the summation is over all $\mathbf{q}$ that contain the intensity samples of interest. In our case we elected to plot the radially averaged profile of SNR and so the $\mathbf{q}$ values of interest are those that fell within radial shells and correspond to valid intensity samples, *i.e.* the intensity data at that location in reciprocal space are not missing. A region of missing data of radius equal to the first Bragg order (3 voxels in this case) was also implemented at the center of the 3D diffracted intensity volume to simulate the effect of the central detector gap, present in order to let the direct X-ray beam pass through. A central slice of the 3D Fourier space volume for the PSII and CatB molecule generated with the above procedure and averaged over 100 2D patterns is shown in Figs. 12 and 15, respectively. The radially averaged SNR from intensity samples of the entire 3D volume, calculated separately for the Bragg and inter-Bragg samples, is plotted alongside the respective slices.

The IPA reconstruction parameters for both the PSII and CatB molecule are kept the same as before, as described in Section 4.2. The intensity values at the missing data regions in

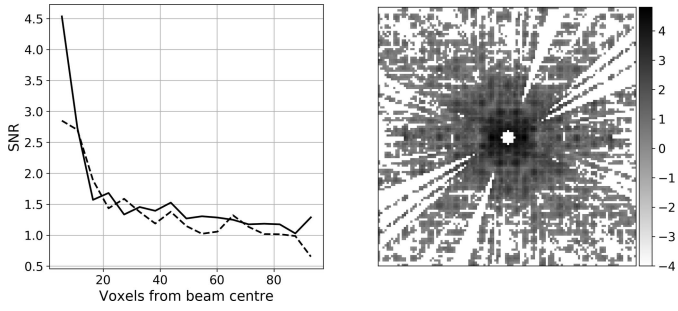

Figure 12
(Left) Radially averaged SNR for the 3D merged diffracted intensity from an ensemble of 100 2D noisy diffraction patterns of edgy PSII crystals. The radially averaged SNR are calculated for Bragg (dashed) and inter-Bragg (solid) locations. (Right) One central 2D slice of the 3D merged diffracted intensity.

reciprocal space are allowed to float during the reconstruction process. The correct support is still assumed and applied as in the previous section. The positivity constraint is again not applied. The values of the intensity at regions in reciprocal space where the intensity data are missing or below a value of 1 intensity value units (blank regions in Figs. 12 and 15) are left floating during the reconstruction process. The results of the reconstructions for PSII and CatB are shown in Figs. 13 and 16, respectively. The final reconstructions shown in those figures are obtained by taking the iterate at the iteration where E_I is the minimum. The reconstructed molecular density and shape transforms from noisy data do not converge to the ground truth; however they do not diverge and give completely non-nonsensical values either, even in the presence of high levels of noise and missing data. Additional work on directly modeling noise in the algorithm should improve its ability to handle noise. A final 3D rendering of the ground truth, the reconstruction with noise, the reconstruction without noise, for the two molecules are given in Figs. 14 and 17.

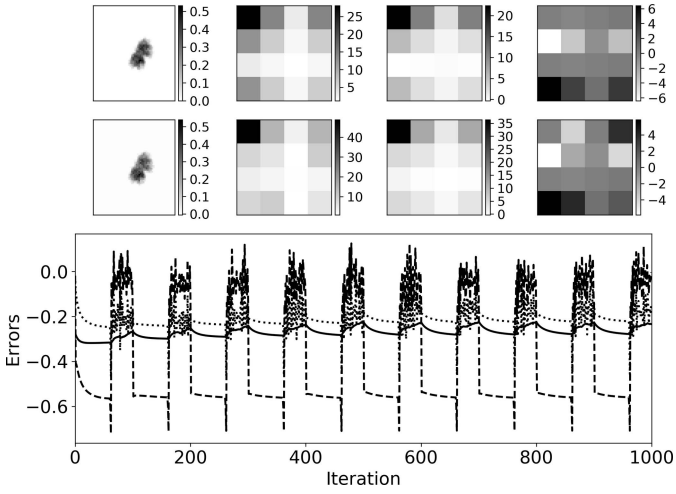

Figure 13
Reconstruction of the PSII molecule given the correct support and the noisy intensity data shown in Fig. 12. Top row shows the ground truth and the second row shows the best reconstruction as gauged by E_I. (Column 1) Projected view of the molecule, (Column 2) $C_{11}(\mathbf{q})$, (Column 3) Re$[C_{12}(\mathbf{q})]$, (Column 4) Im$[C_{12}(\mathbf{q})]$. Only one slice of one period of the 3D $C_{kl}(\mathbf{q})$ functions (the shape transform cell) is shown. The bottom plot shows the reconstruction errors E_f (solid), E_C (dotted) and E_I (dashed) on a log scale as the algorithm proceeds.

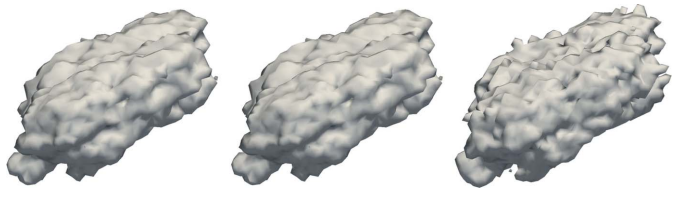

Figure 14
3D isosurface plots of the PSII molecule contoured at 10% of the maximum true density. (Left) Ground truth. (Center) Reconstruction with noiseless intensity data. (Right) Reconstruction with noisy intensity data, generated as described in the text. Both the noisy and noiseless reconstructions assume the correct support.

5. Discussion and conclusions

We developed a reconstruction algorithm that is capable of determining the density of the molecular asymmetric unit when given the averaged coherent diffraction intensity from many crystals of different sizes, shapes and, unlike previous work, with arbitrary molecular occupancies. A mathematical model is formulated that expresses the averaged diffracted intensity in terms of lattice occupancies and the scattering density of the different molecular orientations. The occupancy description can be reformulated in terms of shape transforms, reducing the number of parameters needed to describe the problem while retaining the quantity of interest, which in this case is the scattering density of the asymmetric unit.

The main impetus of shape transform phasing is that diffraction signals can consist of samples both at the Bragg condition and at points between Bragg reflections. The inter-

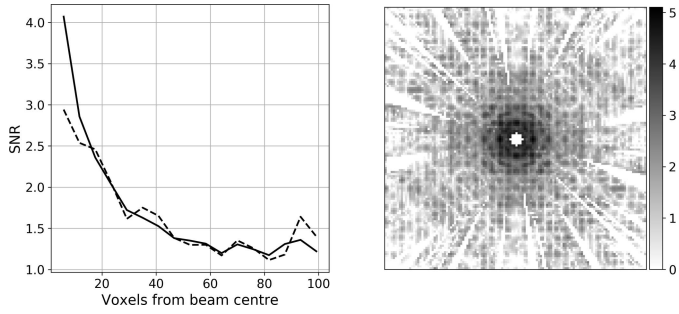

Figure 15
(Left) Radially averaged SNR for the 3D merged diffracted intensity from an ensemble of 100 2D noisy diffraction patterns of edgy CatB crystals. The radially averaged SNR are calculated for Bragg (dashed) and inter-Bragg (solid) locations. (Right) One central 2D slice of the 3D merged diffracted intensity.

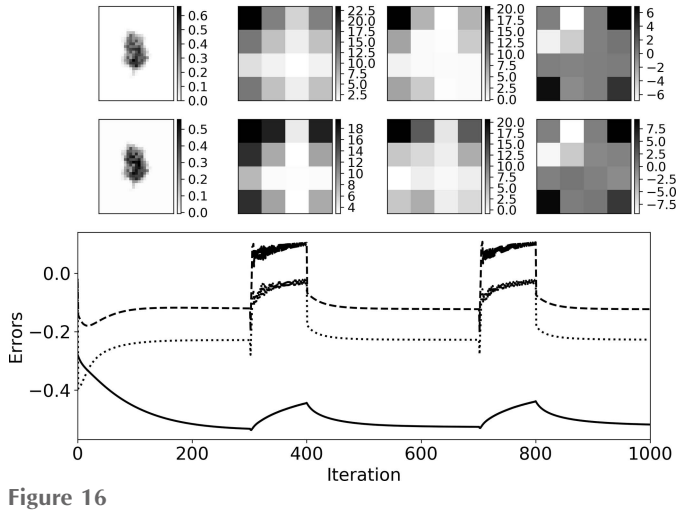

Figure 16
Reconstruction of the CatB molecule given the correct support and the noisy intensity data shown in Fig. 15. Top row shows the ground truth and the second row shows the best reconstruction as gauged by E_I. (Column 1) Projected view of the molecule, (Column 2) $C_{11}(\mathbf{q})$, (Column 3) Re$[C_{12}(\mathbf{q})]$, (Column 4) Im$[C_{12}(\mathbf{q})]$. Only one slice of one period of the 3D $C_{kl}(\mathbf{q})$ functions (the shape transform cell) is shown. The bottom plot shows the reconstruction errors E_f (solid), E_C (dotted) and E_I (dashed) on a log scale as the algorithm proceeds.

Figure 17
3D isosurface plots of the CatB molecule contoured at 10% of the maximum true density. (Left) Ground truth. (Center) Reconstruction with noiseless intensity data. (Right) Reconstruction with noisy intensity data, generated as described in the text. Both the noisy and noiseless reconstructions assume the correct support.

Bragg samples improve the information content significantly compared with the case when only Bragg reflections are available, thus allowing the determination of the electron density of the molecule from the diffracted intensities alone. Through simulations, we showed how our IPA is capable of recovering both the unknown molecular density and the unknown averaged shape transforms in parallel, with good convergence behavior. We have tested the algorithm with intensity data corrupted by Poisson noise along with significant incomplete measurements from the simulated merging of a small number of 2D diffraction patterns. The behavior of the algorithm under these circumstances seems to be stable; however the correct support of the molecule was assumed to be known and therefore the phasing trials with noise performed here are only necessary but not sufficient evidence that the algorithm can work with real data. For a robust implementation, a good noise model or a direct measurement of statistical errors from the serial diffraction data should be incorporated into the reconstruction algorithm, perhaps using techniques explored in other works (Williams *et al.*, 2007; Loh *et al.*, 2010; Dilanian *et al.*, 2010; Martin *et al.*, 2012). A basic noise model in the context of phase retrieval that utilizes signals from shape transforms has been outlined by Chen *et al.* (2014*a*).

The issue of uniqueness for this particular variant of the phase retrieval problem is complicated in general because it depends on (i) the molecular occupancies, (ii) the number of molecular orientations, (iii) the sampling rate of the diffracted intensity and (iv) the shape of the molecule itself. However, simulations suggest that the algorithm can treat the averaged diffraction from crystal ensembles for space groups that have up to eight different molecular orientations per unit cell. Note that we do not need to sample the diffracted intensity according to the size of whole crystals (*i.e.* we do not need to resolve the fringes in the diffraction pattern arising from the shape transform), but rather we only need sufficient sampling with respect to the single molecule. The precise amount of sampling needed to ensure unique reconstruction depends on the constraint ratio Ω.

Although we propose using the averaged diffraction intensity as the input to the reconstruction algorithm for the purpose of improving the SNR and to reduce data volumes, it is conceivable that one may develop an algorithm that utilizes the full set of diffraction patterns individually, without averaging, similar in spirit to frameworks proposed by Loh & Elser (2009), Donatelli *et al.* (2017). With sufficient signal, it may indeed be possible to model the shape transforms in each individual frame via projection operations or expectation-maximization.

The use of distance-minimizing projection operators can be important in IPAs. An initial attempt at the P_M operator utilized a non-distance-minimizing 'constraint-satisfaction' operation for updating the set of functions $\{F_k(\mathbf{q})\}$. The non-optimal operator consisted of a plain scaling of the intensities, suitable for projecting onto a hyper-sphere, but not ideal in general for projecting onto a hyper-ellipsoid. Utilizing this non-distance-minimizing operation in the IPA resulted in unstable reconstructions that often failed to converge. Projections onto ellipsoids have been documented by Stark & Yang (1998), Borwein *et al.* (2018), and in the context of phase retrieval by Morgan *et al.* (2019).

We are working on generalizations to incorporate other kinds of crystal disorder since, under the Born approximation, all diffraction intensities can in principle be expressed in the form $I(\mathbf{q}) = \mathbf{F}^{\dagger}(\mathbf{q})\mathbf{C}(\mathbf{q})\mathbf{F}(\mathbf{q})$, given by the central equation (20) in this article. It may be possible, for example, to include both translational and rotational disorder, as is being explored in other work (Morgan *et al.*, 2019), with the assumption that although disorder breaks the translational symmetry in the shape transforms that we exploit to our advantage here, we expect that many disorder models still retain much redundancy within shells of similar resolution.

Another source that breaks translational symmetry of the shape transforms is from complex wavefront distortions of the incident X-ray beam, as was pointed out by Kirian *et al.* (2015). If we allow the molecular occupancies in our model, $w_{k\alpha n}$, to take on any real values rather than restricting them to be either 0 or 1, then that could in principle model a non-uniform incident-beam profile. The assumption in that case would be that the change in X-ray intensity is negligible across a single molecule. Going one step further, complex $w_{k\alpha n}$ could also be used to emulate phase distortions if, once again, those distortions do not vary significantly from one molecule to the next. Our formulation might also allow for the K objects to be different, although the constraint ratio for that case will be reduced and is yet to be worked out.

APPENDIX *A*
Properties of the averaged shape transform

We show here that the averaged shape transforms satisfy $C_{kl}(\mathbf{q} - \mathbf{g}_{\mathbf{h}}) = C_{kl}(\mathbf{q})$ for all k, l and $\mathbf{h}$, *i.e.* the averaged shape transform functions are periodic in reciprocal space.

Let the real-space lattice points be

$$\mathbf{r}_{\alpha} = \alpha_1\mathbf{a}_1 + \alpha_2\mathbf{a}_2 + \alpha_3\mathbf{a}_3 \tag{65}$$

and the reciprocal-space lattice points be

$$\mathbf{g}_{\mathbf{h}} = h_1\mathbf{b}_1 + h_2\mathbf{b}_2 + h_3\mathbf{b}_3 \tag{66}$$

where the reciprocal-lattice vectors are related to the real-space lattice vectors via

$$\mathbf{b}_1 = 2\pi \frac{\mathbf{a}_2 \times \mathbf{a}_3}{\mathbf{a}_1 \cdot (\mathbf{a}_2 \times \mathbf{a}_3)}$$
$$\mathbf{b}_2 = 2\pi \frac{\mathbf{a}_3 \times \mathbf{a}_1}{\mathbf{a}_2 \cdot (\mathbf{a}_3 \times \mathbf{a}_1)}$$
$$\mathbf{b}_3 = 2\pi \frac{\mathbf{a}_1 \times \mathbf{a}_2}{\mathbf{a}_3 \cdot (\mathbf{a}_1 \times \mathbf{a}_2)}.$$

It follows that

$$\mathbf{b}_i \cdot \mathbf{a}_j = 2\pi\delta_{ij} \tag{67}$$

where δ_{ij} is the Kronecker delta function ($\delta_{ij} = 1$ for $i = j$ and $\delta_{ij} = 0$ for $i \neq j$).

Now

$$C_{kl}(\mathbf{q} - \mathbf{g}_\mathbf{h}) = \sum_{\alpha}^{\infty}\sum_{\beta}^{\infty}\langle w_{k\alpha n} w_{l\beta n}\rangle_n \exp[-i(\mathbf{q} - \mathbf{g}_\mathbf{h}) \cdot (\mathbf{r}_\alpha - \mathbf{r}_\beta)] \tag{68}$$

$$= \sum_{\alpha}^{\infty}\sum_{\beta}^{\infty}\langle w_{k\alpha n} w_{l\beta n}\rangle_n \exp[-i\mathbf{q} \cdot (\mathbf{r}_\alpha - \mathbf{r}_\beta)] \exp[i\mathbf{g}_\mathbf{h} \cdot (\mathbf{r}_\alpha - \mathbf{r}_\beta)] \tag{69}$$

$$= \sum_{\alpha}^{\infty}\sum_{\beta}^{\infty}\langle w_{k\alpha n} w_{l\beta n}\rangle_n \exp[-i\mathbf{q} \cdot (\mathbf{r}_\alpha - \mathbf{r}_\beta)]$$
$$= C_{kl}(\mathbf{q}), \tag{70}$$

since the value of the last exponential in equation (69) is unity, as

$$\begin{aligned}\mathbf{g}_\mathbf{h} \cdot (\mathbf{r}_\alpha - \mathbf{r}_\beta) &= (h_1\mathbf{b}_1 + h_2\mathbf{b}_2 + h_3\mathbf{b}_3) \cdot [(\alpha_1 - \beta_1)\mathbf{a}_1 \\ &\quad + (\alpha_2 - \beta_2)\mathbf{a}_2 + (\alpha_3 - \beta_3)\mathbf{a}_3] \\ &= 2\pi[h_1(\alpha_1 - \beta_1) + h_2(\alpha_2 - \beta_2) \\ &\quad + h_3(\alpha_3 - \beta_3)] \\ &= 2\pi m\end{aligned}$$

where m is an integer. The averaged shape transform function $C_{kl}(\mathbf{q})$ is therefore periodic, with the period being referred to in this article as the 'shape transform cell'.

We finally note that the above also shows that the averaged shape transforms are inversion conjugate symmetric with respect to $\mathbf{q}$, *i.e.*

$$C_{kl}(-\mathbf{q}) = C^*_{kl}(\mathbf{q}), \tag{71}$$

since a change of sign in $\mathbf{q}$ is equivalent to taking the complex conjugate of equation (70).

Note that exchanging the indices $\boldsymbol{\alpha}$ and $\boldsymbol{\beta}$ that appear symmetrically in the summations in equation (70) may at first sight suggest $C_{kl}(-\mathbf{q}) = C_{kl}(\mathbf{q})$; however, upon closer inspection we see that the product of the occupancies $w_{k\alpha n}w_{l\beta n}$ and $w_{k\beta n}w_{l\alpha n}$ may not necessarily be equal.

APPENDIX *B*
Constraint ratio

The constraint ratio Ω is defined as the ratio of the number of independent measurements to the number of independent unknown quantities. It is necessary, but not sufficient, to have $\Omega \geq 1$ in order to obtain a unique solution to any phase retrieval problem. In order to count independent measurements, it is helpful to look to the Fourier transform of the diffraction intensities, which is equal to the autocorrelation of the object densities, which is finite in extent. For a single, isolated object, the number of independent measurements of its diffraction intensity is estimated as the number of samples in the non-zero region of the autocorrelation of the object, denoted here by $\mathcal{A}$, divided by two, to account for the centrosymmetry of the autocorrelation. The number of independent unknown parameters is the number of samples in the object, denoted here by $\mathcal{S}$. Assuming that the diffraction intensities are sampled with sufficient frequency, the constraint ratio for a single particle, $\Omega_{\rm sp}$, is equal to half the volume of the autocorrelation of the particle over the volume of the particle (Elser & Millane, 2008), *i.e.*

$$\Omega_{\rm sp} = \frac{\mathcal{A}/2}{\mathcal{S}}. \tag{72}$$

In 3D, the constraint ratio is greater than or equal to 4, where the worst case of $\Omega = 4$ is for an object with a support that is convex and centrosymmetric.

Previous considerations of the constraint ratio for crystalline objects took into account only crystals comprising full unit cells without consideration of individual molecular occupancies (Millane & Chen, 2014; Millane & Arnal, 2015; Morgan *et al.*, 2019). We now investigate the constraint ratio for the case when it is not assumed that the crystal is comprised of full unit cells. The differences in the problem that we consider here compared with previous studies are that (i) we have an ensemble of crystals and the intensity data are the averaged intensity from this ensemble, and (ii) each crystal in the ensemble can have molecules that are absent when compared with the nominal unit-cell configuration.

Taking the inverse Fourier transform of the average diffracted intensity $I(\mathbf{q})$ in equation (7) returns the average over crystal autocorrelations:

$$\begin{aligned}A(\mathbf{r}) &= \langle A_n(\mathbf{r})\rangle_n \\ &= \sum_{\alpha}^{\infty}\sum_{\beta}^{\infty}\sum_{k=1}^{K}\sum_{l=1}^{K} W_{k\alpha l\beta}[f_l(\mathbf{r} - \mathbf{r}_\beta) \star f_k(\mathbf{r} - \mathbf{r}_\alpha)] \qquad (73)\end{aligned}$$

$$= \sum_{\alpha}^{\infty}\sum_{\beta}^{\infty}\sum_{k=1}^{K}\sum_{l=1}^{K} W_{k\alpha l\beta}\{f_l(\mathbf{r}) \star f_k[\mathbf{r} - (\mathbf{r}_\alpha - \mathbf{r}_\beta)]\} \qquad (74)$$

where $\star$ denotes the correlation operation. The above expression consists of a weighted superposition of translated copies of the autocorrelations $A_{kk}(\mathbf{r}) = f_k(\mathbf{r}) \star f_k(\mathbf{r})$ and cross-correlations $A_{kl}(\mathbf{r}) = f_k(\mathbf{r}) \star f_l(\mathbf{r})$. With this notation we write the compact form

$$A(\mathbf{r}) = \sum_{\alpha}^{\infty}\sum_{\beta}^{\infty}\sum_{k=1}^{K}\sum_{l=1}^{K} W_{k\alpha l\beta} A_{kl}[\mathbf{r} - (\mathbf{r}_\alpha - \mathbf{r}_\beta)]. \tag{75}$$

We can also express $A(\mathbf{r})$ in terms of the 'averaged shape functions', $c_{kl}(\mathbf{r})$, which is just the inverse Fourier transform of $C_{kl}(\mathbf{q})$. In that case we get

$$A(\mathbf{r}) = \sum_{k=1}^{K}\sum_{l=1}^{K} c_{kl}(\mathbf{r}) \otimes A_{kl}(\mathbf{r}) \tag{76}$$

where

$$c_{kl}(\mathbf{r}) = \sum_{\alpha}^{\infty}\sum_{\beta}^{\infty} W_{k\alpha l\beta}\delta[\mathbf{r} - (\mathbf{r}_{\alpha} - \mathbf{r}_{\beta})]. \tag{77}$$

The number of non-zero weights $W_{k\alpha l\beta}$ that multiply with the Dirac delta functions in equation (77) represent the total amount of information needed to uniquely determine $c_{kl}(\mathbf{r})$. This number scales with the sixth power of the linear crystal size as discussed in Section 2.1, and if our objective is to determine the set of all $W_{k\alpha l\beta}$ then we will almost certainly have a constraint ratio of much less than one ($\Omega \ll 1$). However, the objective in our case is to determine the molecular densities, and hence we need only consider the sampling frequency of the diffracted intensity that is required to determine the density of the molecule, which we expect is well below the critical sampling frequency for determining a whole crystal. If we sample the diffraction intensities on a uniform grid in the crystal basis, with a subset of the grid points coinciding exactly with the Bragg conditions, then the shape function given by equation (77) will be aliased such that the delta functions overlap exactly. The weights associated with those delta functions that overlap will sum to form a new set of weights $W'_{k\alpha l\beta}$. In such a case, equation (77) maintains the same form, but the number of new unknown weights $W'_{k\alpha l\beta}$ needed to specify our data is reduced. This is the basis of the reduction in the number of parameters when the problem is formulated in terms of the averaged shape transform (Section 2.2) as opposed to the occupancy matrix (Section 2.1).

For finite crystals, the lowest value of Ω corresponds to an incoherent average over the diffracted intensities of all molecular orientations, which can arise from hypothetical crystals with very low occupancies that are uniformly random and diffract like a gas of oriented molecules in the limiting case. In that scenario, it was concluded by Millane & Chen (2014) that unique recovery of a 3D molecule of any shape from the averaged diffracted intensity is possible if the number of molecular orientations is less than or equal to 4, where 4 is the marginal case, since Ω is bounded below by 4 in 3D for a single isolated object as previously mentioned. Using the notation introduced in equation (72) for the constraint ratio of a single particle, $\Omega_{\rm sp}$, the constraint ratio for the worst case can be expressed as

$$\Omega_{\rm worst} = \frac{\mathcal{A}/(2K)}{\mathcal{S}} = \frac{\Omega_{\rm sp}}{K}. \tag{78}$$

The best-case scenario is another hypothetical situation in which all molecules are spaced sufficiently far apart to give direct access to all the cross-correlation terms $A_{kl}(\mathbf{r})$, $k \neq l$, without overlap, solely from the diffracted intensity, which is analogous to holographic techniques studied elsewhere (Martin *et al.*, 2013). In this case the constraint ratio increases due to the additional volumes of the cross-correlations, which we assume for simplicity in the analysis here to have the same support volume as the autocorrelations. Since the cross-correlations are not centrosymmetric like the autocorrelations, and since each of the autocorrelations is identical in 3D, the number of independent measurements grows from $\mathcal{A}/(2K)$ in the worst case to $\mathcal{A}/2 + (K^2 - K)\mathcal{A}/2$ in the best case. The constraint ratio for the best case is therefore given by

$$\Omega_{\rm best} = \frac{\mathcal{A}[1 + (K^2 - K)]/2}{\mathcal{S}} = (K^2 - K + 1)\Omega_{\rm sp}. \tag{79}$$

The ranges of Ω for molecules arranged in three different configurations are summarized in Table 1. The three configurations are: (i) single particle – only a single molecule in the X-ray beam; (ii) perfect crystals – crystals that can be described by a single type of unit cell, *i.e.* no random edge truncations; (iii) edgy crystals – crystals with arbitrary molecular occupancies. Note that we assume the number of unknown weights $W'_{k\alpha l\beta}$ is sufficiently small in comparison with $\mathcal{S}$ that the weights can be ignored when counting the amount of unknowns in determining the constraint ratio, *i.e.* the number of parameters in the molecular density is much greater than the number of parameters needed to describe the averaged shape transforms.

Table 1
The constraint ratio for objects in various configurations and reciprocal-space samplings.

f is the fraction of the unit cell (well-defined for perfect crystals) occupied by the molecule, K is the number of unique orientations of the molecule in the crystal. s is the sampling factor in reciprocal space relative to the Bragg sampling.

	$s = 1$	$s \geq 2$
Single particles	$\Omega = 1/2$	$\Omega = \Omega_{\rm sp}$
Perfect crystals	$\Omega = 1/(2f)$	$1/(2f) \leq \Omega \leq \Omega_{\rm sp}$
Edgy crystals	$1/2 \leq \Omega \leq 1$	$\Omega_{\rm sp}/K \leq \Omega \leq (K^2 - K + 1)\Omega_{\rm sp}$

APPENDIX C
Minimum-change least squares

Consider matrices $\mathbf{I}$ ($M \times 1$), $\mathbf{Z}$ ($M \times N$) and $\mathbf{C}^{(i)}$ ($N \times 1$) for some integers M and N, related by

$$\mathbf{I} = \mathbf{Z}\mathbf{C}^{(i)}. \tag{80}$$

Note that $\mathbf{I}$ is not the identity matrix but a vector that holds the diffracted intensity values in the context of shape transform phasing. A new estimate of $\mathbf{C}$, denoted by $\mathbf{C}^{(i+1)}$, is given by

$$\mathbf{C}^{(i+1)} = \mathbf{Z}^{+}\mathbf{I}, \tag{81}$$

where $\mathbf{Z}^{+}$ is the pseudo-inverse of $\mathbf{Z}$ as defined in equation (38). In this case the 2-norm of the new estimate is minimized:

$$\min ||\mathbf{C}^{(i+1)}||_2. \tag{82}$$

This is the 'minimum-norm' least-squares solution.

Instead of finding a $\mathbf{C}$ closest to the origin, an often more sensible minimization is to find a $\mathbf{C}$ that is closest to a previous estimate of $\mathbf{C}$. Our problem then becomes

$$\min ||\mathbf{C}^{(i+1)} - \mathbf{C}^{(i)}||_2 \tag{83}$$

subject to

$$\mathbf{I} = \mathbf{Z}\mathbf{C}^{(i+1)}. \tag{84}$$

The trick to solving this is to utilize the result from the minimum-norm solution. Write

$$\mathbf{I} = \mathbf{Z}[\mathbf{C}^{(i+1)} - \mathbf{C}^{(i)} + \mathbf{C}^{(i)}]$$

and rearrange to get

$$\mathbf{I} - \mathbf{Z}\mathbf{C}^{(i)} = \mathbf{Z}[\mathbf{C}^{(i+1)} - \mathbf{C}^{(i)}]. \tag{85}$$

Comparing the form of equations (80) and (85), we can immediately utilize equation (81) to write

$$\mathbf{C}^{(i+1)} - \mathbf{C}^{(i)} = \mathbf{Z}^{+}[\mathbf{I} - \mathbf{Z}\mathbf{C}^{(i)}], \tag{86}$$

giving the 'minimum-change' least-squares solution as

$$\mathbf{C}^{(i+1)} = \mathbf{C}^{(i)} + \mathbf{Z}^{+}[\mathbf{I} - \mathbf{Z}\mathbf{C}^{(i)}]. \tag{87}$$

APPENDIX *D*
Positive semi-definite projection

Given a Hermitian matrix $\mathbf{A}$ we seek a matrix $\mathbf{B}$ that is PSD such that the Frobenius norm $||\mathbf{A} - \mathbf{B}||_{\rm F} = (\sum_i \sum_j |\mathbf{A}_{ij} - \mathbf{B}_{ij}|^2)^{1/2}$ is as small as possible. In other words, we want to minimize $||\mathbf{A} - \mathbf{B}||_{\rm F}$ such that the eigenvalues of $\mathbf{B}$ are all non-negative. In this appendix, we first show that the Frobenius norm of the difference between two matrices is always minimized when the two matrices have the same set of eigenvectors. Then imposing the condition for the eigenvalues of $\mathbf{B}$ to be non-negative leads to the desired result.

Using Dirac notation, the Frobenius norm can be expressed as

$$\begin{aligned} ||\mathbf{A} - \mathbf{B}||_{\rm F}^2 &= {\rm tr}[(\mathbf{A} - \mathbf{B})(\mathbf{A} - \mathbf{B})^{\dagger}] \\ &= \sum_i \langle i|(\mathbf{A} - \mathbf{B})(\mathbf{A} - \mathbf{B})^{\dagger}|i\rangle, \end{aligned} \tag{88}$$

where tr(·) denotes the trace operation. The trace is invariant to similarity transformations, and in particular, unitary transformations. We can therefore write the above in terms of the eigenbasis of the, so far, unknown $\mathbf{B}$,

$$\mathbf{B}|n\rangle = \lambda_n^{(B)}|n\rangle, \tag{89}$$

where the eigenvectors are normalized such that

$$\langle n|m\rangle = \delta_{nm}. \tag{90}$$

Writing the Frobenius norm in this basis gives

$$||\mathbf{A} - \mathbf{B}||_{\rm F}^2 = \sum_n \langle n|\mathbf{A}^2 - 2\lambda_n^{(B)}\mathbf{A} + \lambda_n^{(B)^2}|n\rangle. \tag{91}$$

We need to minimize equation (91) subject to the constraint that the eigenvectors $|n\rangle$ satisfy the normalization condition given by equation (90), and that the eigenvalues $\lambda_n^{(B)} \geq 0$. Using Lagrange multipliers β_1 and β_2 for the above two constraints, respectively, we can write down the objective function, L, for our optimization problem as

$$L = ||\mathbf{A} - \mathbf{B}||_{\rm F}^2 - \beta_1\langle n|n\rangle - \beta_2\Big([\lambda_n^{(B)}]^{1/2} - \{[\lambda_n^{(B)}]^{1/2}\}^{*}\Big). \tag{92}$$

Minimizing first with respect to the eigenvectors, we vary L with respect to the left eigenvectors, $\langle n|$, to find

$$\frac{\delta L}{\delta\langle n|} = [\mathbf{A}^2 - 2\lambda_n^{(B)}\mathbf{A} + \lambda_n^{(B)^2}]|n\rangle - \beta_1|n\rangle. \tag{93}$$

Setting equation (93) to zero yields

$$\mathbf{A}[\mathbf{A} - 2\lambda_n^{(B)}]|n\rangle = [\beta_1 - \lambda_n^{(B)^2}]|n\rangle \tag{94}$$

which is an eigenvalue equation

$$\mathbf{C}|n\rangle = \alpha_n|n\rangle, \tag{95}$$

where $\mathbf{C} = \mathbf{A}[\mathbf{A} - 2\lambda_n^{(B)}]$ and $\alpha_n = \beta_1 - \lambda_n^{(B)^2}$. Since $\mathbf{AC} = \mathbf{CA}$ and that $\mathbf{A}$ and $\mathbf{C}$ are both Hermitian, the eigenvectors $|n\rangle$ must be common to the matrices $\mathbf{C}$ and $\mathbf{A}$. Furthermore, since $|n\rangle$ was originally the eigenvector of $\mathbf{B}$, $\mathbf{A}$ and $\mathbf{B}$ can therefore share the same set of eigenvectors.

In light of this revelation, equation (91) can be written as

$$\begin{aligned} ||\mathbf{A} - \mathbf{B}||_{\rm F}^2 &= \sum_n \langle n|\lambda_n^{(A)^2} - 2\lambda_n^{(A)}\lambda_n^{(B)} + \lambda_n^{(B)^2}|n\rangle \\ &= \sum_n [\lambda_n^{(A)} - \lambda_n^{(B)}]^2, \end{aligned} \tag{96}$$

where $\lambda_n^{(A)}$ is the nth eigenvalue of $\mathbf{A}$. Now we see that the Frobenius norm is minimized if

$$\lambda_n^{(B)} = \begin{cases} \lambda_n^{(A)} & \lambda_n^{(A)} \geq 0 \\ 0 & \lambda_n^{(A)} < 0 \end{cases} \tag{97}$$

when the constraint $\lambda_n^{(B)} \geq 0$ is enforced. This is the desired operation as required. The projection operator therefore consists of calculating the eigenvalues and eigenvectors of $\mathbf{A}$, setting any negative eigenvalues to 0, and transforming using the original eigenvectors to form the matrix $\mathbf{B}$. The matrix $\mathbf{B}$ will then be the closest PSD matrix to $\mathbf{A}$ measured in terms of the Frobenius norm.

APPENDIX *E*
Ellipsoidal projection

Given the equation

$$I_{\rm data} = \sum_{k=1}^{K} \lambda_k |F_k|^2 = \sum_{k=1}^{K} \lambda_k (x_k^2 + y_k^2), \tag{98}$$

where $F_k = x_k + iy_k$, we seek the modification to an arbitrary complex number $F_k' = x_k' + iy_k'$ such that equation (98) is satisfied while minimizing the Euclidean distance $\sum_{k=1}^{K}[(x_k - x_k')^2 + (y_k - y_k')^2]$. Using a Lagrange multiplier β, we can write down the objective function:

$$\begin{aligned} L = &\sum_{k=1}^{K}\Big[(x_k - x_k')^2 + (y_k - y_k')^2\Big] \\ &+ \beta\Big[\sum_{k=1}^{K} \lambda_k (x_k^2 + y_k^2) - I_{\rm data}\Big]. \end{aligned} \tag{99}$$

Differentiating with respect to x_k and y_k and setting those expressions to zero yields

$$0 = \frac{\partial L}{\partial x_k} = 2x_k(1+\beta\lambda_k) - 2x'_k$$
$$0 = \frac{\partial L}{\partial y_k} = 2y_k(1+\beta\lambda_k) - 2y'_k$$

so that

$$x_k = \frac{x'_k}{1+\beta\lambda_k} \tag{100}$$

$$y_k = \frac{y'_k}{1+\beta\lambda_k}. \tag{101}$$

Substituting these into the constraint equation (98) gives

$$I_{\rm data} = \sum_{k=1}^{K} \frac{\lambda_k |F'_k|^2}{(1+\beta\lambda_k)^2}, \tag{102}$$

which can be numerically solved for the optimum β, as explained in Section 3.3.3, and substituted into equations (100) and (101) to yield the real and imaginary parts of the F_k that satisfies equation (98) but is also the closest to the starting point F'_k measured in terms of the Euclidean distance.

Acknowledgements

We would like to thank Romain Arnal, Kartik Ayyer, Richard Bean, Ken Beyerlein, Henry Chapman, Andrew Martin, Derek Mendez, Rick Millane, Andrew Morgan, Kanupriya Pande, John Spence, Oleksandr Yefanov and Nadia Zatsepin for many helpful discussions. We would also like to thank the two anonymous referees for their time in reading through this lengthy manuscript and providing much insightful feedback.

Funding information

RAK and JPJC acknowledge support from NSF STC Award DBI-1231306, RAK, KES and JPJC acknowledge support from NSF Award DBI-1565180, JJD acknowledges support from the Advanced Scientific Computing Research and the Basic Energy Sciences programs, which are supported by the Office of Science of the US Department of Energy under Contract DE-AC02-05CH11231.

References

Ayyer, K., Yefanov, O. M., Oberthür, D., Roy-Chowdhury, S., Galli, L., Mariani, V., Basu, S., Coe, J., Conrad, C. E., Fromme, R., Schaffer, A., Dörner, K., James, D., Kupitz, C., Metz, M., Nelson, G., Xavier, P. L., Beyerlein, K. R., Schmidt, M., Sarrou, I., Spence, J. C. H., Weierstall, U., White, T. A., Yang, J.-H., Zhao, Y., Liang, M., Aquila, A., Hunter, M. S., Robinson, J. S., Koglin, J. E., Boutet, S., Fromme, P., Barty, A. & Chapman, H. N. (2016). *Nature*, **530**, 202–206.

Borwein, J. M., Lindstrom, S. B., Sims, B., Schneider, A. & Skerritt, M. P. (2018). *Set-Valued Var. Anal.* **26**, 385–403.

Boutet, S. & Robinson, I. K. (2008). *J. Synchrotron Rad.* **15**, 576–583.

Chapman, H. N., Fromme, P., Barty, A., White, T. A., Kirian, R. A., Aquila, A., Hunter, M. S., Schulz, J., DePonte, D. P., Weierstall, U., Doak, R. B., Maia, F. R. N. C., Martin, A. V., Schlichting, I., Lomb, L., Coppola, N., Shoeman, R. L., Epp, S. W., Hartmann, R., Rolles, D., Rudenko, A., Foucar, L., Kimmel, N., Weidenspointner, G., Holl, P., Liang, M., Barthelmess, M., Caleman, C., Boutet, S., Bogan, M. J., Krzywinski, J., Bostedt, C., Bajt, S., Gumprecht, L., Rudek, B., Erk, B., Schmidt, C., Hömke, A., Reich, C., Pietschner, D., Strüder, L., Hauser, G., Gorke, H., Ullrich, J., Herrmann, S., Schaller, G., Schopper, F., Soltau, H., Kühnel, K., Messerschmidt, M., Bozek, J. D., Hau-Riege, S. P., Frank, M., Hampton, C. Y., Sierra, R. G., Starodub, D., Williams, G. J., Hajdu, J., Timneanu, N., Seibert, M. M., Andreasson, J., Rocker, A., Jönsson, O., Svenda, M., Stern, S., Nass, K., Andritschke, R., Schröter, C., Krasniqi, F., Bott, M., Schmidt, K. E., Wang, X., Grotjohann, I., Holton, J. M., Barends, T. R. M., Neutze, R., Marchesini, S., Fromme, R., Schorb, S., Rupp, D., Adolph, M., Gorkhover, T., Andersson, I., Hirsemann, H., Potdevin, G., Graafsma, H., Nilsson, B. & Spence, J. C. H. (2011). *Nature*, **470**, 73–77.

Chen, J. P. J., Arnal, R. D., Morgan, A. J., Bean, R. J., Beyerlein, K. R., Chapman, H. N., Bones, P. J., Millane, R. P. & Kirian, R. A. (2016). *J. Opt.* **18**, 114003.

Chen, J. P. J. & Millane, R. P. (2014). *J. Opt. Soc. Am. A*, **31**, 1730–1737.

Chen, J. P. J., Spence, J. C. H. & Millane, R. P. (2014*a*). *Acta Cryst.* A**70**, 143–153.

Chen, J. P. J., Spence, J. C. H. & Millane, R. P. (2014*b*). *Acta Cryst.* A**70**, 154–161.

Dilanian, R. A., Streltsov, V. A., Quiney, H. M. & Nugent, K. A. (2013). *Acta Cryst.* A**69**, 108–118.

Dilanian, R. A., Williams, G. J., Whitehead, L. W., Vine, D. J., Peele, A. G., Balaur, E., McNulty, I., Quiney, H. M. & Nugent, K. A. (2010). *New J. Phys.* **12**, 093042.

Donatelli, J. J., Sethian, J. A. & Zwart, P. H. (2017). *Proc. Natl Acad. Sci. USA*, **114**, 7222–7227.

Elser, V. (2003*a*). *J. Opt. Soc. Am. A*, **20**, 40–55.

Elser, V. (2003*b*). *J. Phys. A Math. Gen.* **36**, 2995–3007.

Elser, V. (2013). *Acta Cryst.* A**69**, 559–569.

Elser, V. (2017). *J. Glob. Optim.* **68**, 329–355.

Elser, V. & Millane, R. P. (2008). *Acta Cryst.* A**64**, 273–279.

Emma, P., Akre, R., Arthur, J., Bionta, R., Bostedt, C., Bozek, J., Brachmann, A., Bucksbaum, P., Coee, R., Decker, F. J., Ding, Y., Dowell, D., Edstrom, S., Fisher, A., Frisch, J., Gilevich, S., Hastings, J., Hays, G., Hering, P., Huang, Z., Iverson, R., Loos, H., Messerschmidt, M., Miahnahri, A., Moeller, S., Nuhn, H. D., Pile, G., Ratner, D., Rzepiela, J., Schultz, D., Smith, T., Stefan, P., Tompkins, H., Turner, J., Welch, J., White, W., Wu, J., Yocky, G. & Galayda, J. (2010). *Nat. Photonics*, **4**, 641–647.

Fienup, J. R. (1982). *Appl. Opt.* **21**, 2758–2769.

Green, D. W., Ingram, V. M. & Perutz, M. F. (1954). *Proc. R. Soc. London Ser. A*, **225**, 287–307.

Higham, N. J. (1988). *Linear Algebra Appl.* **103**, 103–118.

Kirian, R. A., Bean, R. J., Beyerlein, K. R., Barthelmess, M., Yoon, C. H., Wang, F., Capotondi, F., Pedersoli, E., Barty, A. & Chapman, H. N. (2015). *Phys. Rev. X*, **5**, 011015.

Kirian, R. A., Bean, R. J., Beyerlein, K. R., Yefanov, O. M., White, T. A., Barty, A. & Chapman, H. N. (2014). *Philos. Trans. R. Soc. B Biol. Sci.* **369**, 20130331.

Kirian, R. A., Wang, X. Y., Weierstall, U., Schmidt, K. E., Spence, J. C. H., Hunter, M., Fromme, P., White, T. A., Chapman, H. N. & Holton, J. (2010). *Opt. Express*, **18**, 5713–5723.

Liu, H., Zatsepin, N. A. & Spence, J. C. H. (2014). *IUCrJ*, **1**, 19–27.

Loh, N. D., Eisebitt, S., Flewett, S. & Elser, V. (2010). *Phys. Rev. E*, **82**, 061128.

Loh, N. D. & Elser, V. (2009). *Phys. Rev. E*, **80**, 026705.

Luke, D. R. (2005). *Inverse Probl.* **21**, 37–50.

Marchesini, S. (2007). *Rev. Sci. Instrum.* **78**, 001301.

Martin, A. V., Morgan, A. J., Ekeberg, T., Loh, N. D., Maia, F. R. N. C., Wang, F., Spence, J. C. H. & Chapman, H. N. (2013). *Opt. Express*, **21**, 15102–15112.

Martin, A. V., Wang, F., Loh, N. D., Ekeberg, T., Maia, F. R. N. C., Hantke, M., van der Schot, G., Hampton, C. Y., Sierra, R. G., Aquila, A., Bajt, S., Barthelmess, M., Bostedt, C., Bozek, J. D.,

Coppola, N., Epp, S. W., Erk, B., Fleckenstein, H., Foucar, L., Frank, M., Graafsma, H., Gumprecht, L., Hartmann, A., Hartmann, R., Hauser, G., Hirsemann, H., Holl, P., Kassemeyer, S., Kimmel, N., Liang, M., Lomb, L., Marchesini, S., Nass, K., Pedersoli, E., Reich, C., Rolles, D., Rudek, B., Rudenko, A., Schulz, J., Shoeman, R. L., Soltau, H., Starodub, D., Steinbrener, J., Stellato, F., Strüder, L., Ullrich, J., Weidenspointner, G., White, T. A., Wunderer, C. B., Barty, A., Schlichting, I., Bogan, M. J. & Chapman, H. N. (2012). *Opt. Express*, **20**, 16650–16661.

Millane, R. P. & Arnal, R. D. (2015). *Acta Cryst.* A**71**, 592–598.

Millane, R. P. & Chen, J. P. J. (2014). *Philos. Trans. R. Soc. B Biol. Sci.* **369**, 20130498.

Millane, R. P. & Lo, V. L. (2013). *Acta Cryst.* A**69**, 517–527.

Morgan, A. J., Ayyer, K., Barty, A., Chen, J. P. J., Ekeberg, T., Oberthuer, D., White, T. A., Yefanov, O. & Chapman, H. N. (2019). *Acta Cryst.* A**75**, 25–40.

Redecke, L., Nass, K., DePonte, D. P., White, T. A., Rehders, D., Barty, A., Stellato, F., Liang, M., Barends, T. R. M., Boutet, S., Williams, G. J., Messerschmidt, M., Seibert, M. M., Aquila, A., Arnlund, D., Bajt, S., Barth, T., Bogan, M. J., Caleman, C., Chao, T. C., Doak, R. B., Fleckenstein, H., Frank, M., Fromme, R., Galli, L., Grotjohann, I., Hunter, M. S., Johansson, L. C., Kassemeyer, S., Katona, G., Kirian, R. A., Koopmann, R., Kupitz, C., Lomb, L., Martin, A. V., Mogk, S., Neutze, R., Shoeman, R. L., Steinbrener, J., Timneanu, N., Wang, D., Weierstall, U., Zatsepin, N. A., Spence, J. C. H., Fromme, P., Schlichting, I., Duszenko, M., Betzel, C. & Chapman, H. N. (2013). *Science*, **339**, 227–230.

Sayre, D. (1952). *Acta Cryst.* **5**, 843.

Schlichting, I. (2015). *IUCrJ*, **2**, 246–255.

Schlichting, I. (2017). *IUCrJ*, **4**, 516–517.

Son, S.-K., Chapman, H. N. & Santra, R. (2011). *Phys. Rev. Lett.* **107**, 218102.

Spence, J. C. H. (2017). *IUCrJ*, **4**, 322–339.

Spence, J. C. H., Kirian, R. A., Wang, X. Y., Weierstall, U., Schmidt, K. E., White, T. A., Barty, A., Chapman, H. N., Marchesini, S. & Holton, J. (2011). *Opt. Express*, **19**, 2866–2873.

Stark, H. & Yang, Y. (1998). *Vector Space Projections*. New York: John Wiley & Sons.

Umena, Y., Kawakami, K., Shen, J.-R. & Kamiya, N. (2011). *Nature*, **473**, 55–60.

Williams, G., Pfeifer, M., Vartanyants, I. & Robinson, I. (2007). *Acta Cryst.* A**63**, 36–42.

Williams, S. R., Dilanian, R. A., Quiney, H. M. & Martin, A. V. (2017). *Crystals*, **7**, 220.

Yefanov, O., Gati, C., Bourenkov, G., Kirian, R. A., White, T. A., Spence, J. C. H., Chapman, H. N. & Barty, A. (2014). *Philos. Trans. R. Soc. B Biol. Sci.* **369**, 20130333.

Zatsepin, N. A. (2018). *Protein Crystallography: Challenges and Practical Solutions*, edited by K. Beis & G. Evans, ch. 8, pp. 181–224.